JGP Journal of General Physiology

ARTICLE

Differential regulation of BK channels by fragile X mental retardation protein

Aravind Kshatri[1,2], Alejandro Cerrada[1,2], Roger Gimeno[1,2], David Bartolomé-Martín[1,2], Patricio Rojas[3], and Teresa Giraldez[1,2]

Fragile X mental retardation protein (FMRP) is an RNA-binding protein prominently expressed in neurons. Missense mutations or complete loss of FMRP can potentially lead to fragile X syndrome, a common form of inherited intellectual disability. In addition to RNA regulation, FMRP was also proposed to modulate neuronal function by direct interaction with the large conductance Ca^{2+}- and voltage-activated potassium channel (BK) β_4 regulatory subunits (BKβ_4). However, the molecular mechanisms underlying FMRP regulation of BK channels were not studied in detail. We have used electrophysiology and super-resolution stochastic optical reconstruction microscopy (STORM) to characterize the effects of FMRP on pore-forming BKα subunits, as well as the association with regulatory subunits BKβ_4. Our data indicate that, in the absence of coexpressed β_4, FMRP alters the steady-state properties of BKα channels by decreasing channel activation and deactivation rates. Analysis using the Horrigan-Aldrich model revealed alterations in the parameters associated with channel opening (L_0) and voltage sensor activation (J_0). Interestingly, FMRP also altered the biophysical properties of BK$\alpha\beta_4$ channels favoring channel opening, although not as dramatically as BKα. STORM experiments revealed clustered multi-protein complexes, consistent with FMRP interacting not only to BK$\alpha\beta_4$ but also to BKα. Lastly, we found that a partial loss-of-function mutation in FMRP (R138Q) counteracts many of its functional effects on BKα and BK$\alpha\beta_4$ channels. In summary, our data show that FMRP modulates the function of both BKα and BK$\alpha\beta_4$ channels.

Introduction

The large conductance Ca^{2+}-activated potassium (BK) channels are formed by the tetrameric association of channel-forming α subunits that are encoded by the Slo1 or *KCNMA1* gene (Atkinson et al., 1991; Butler et al., 1993). Each BKα subunit is formed by a transmembrane core (S0–S6) and a large cytoplasmic domain containing binding sites for Ca^{2+} and Mg^{2+} ions (for a recent review, see Latorre et al., 2017). The diversity of BKα channels is conferred by their association with auxiliary $\beta_{(1-4)}$ subunits (Knaus et al., 1994; Wallner et al., 1999; Xia et al., 1999; Behrens et al., 2000; Brenner et al., 2000; Uebele et al., 2000). Three main populations of BK channels have been found in central neurons: the noninactivating iberiotoxin-sensitive, fast-gated "type I" channels, which are formed by BKα subunits; the non-inactivating iberiotoxin-resistant, slow-gated, type II channels, formed by BK$\alpha\beta_4$ complexes; and the iberiotoxin-sensitive inactivating channels including (but not limited to) BK$\alpha\beta_2$ complexes (Reinhart et al., 1989; Bielefeldt et al., 1992; Reinhart and Levitan, 1995; Meera et al., 2000; Faber and Sah, 2003; Whitt et al., 2016). These associations alter BK channel activation and inactivation properties, subcellular trafficking, and pharmacology (Kshatri et al., 2018). As physiological controllers of K^+ efflux timing and duration, BK channels are implicated in a multitude of roles in the central nervous system including regulation of neuronal action potential (AP) shape, firing frequency, and control of neurotransmitter release from presynaptic terminals (Robitaille and Charlton, 1992; Robitaille et al., 1993).

The fragile X mental retardation protein (FMRP) is an RNA-binding protein that regulates translation (Wang et al., 2012), potentially affecting hundreds of mRNAs (Brown et al., 2001; Darnell et al., 2001; Chen et al., 2003; Chen et al., 2014). FMRP is encoded by the *FMR1* gene, which is expressed in many tissues and at high levels in neurons (Devys et al., 1993; Fähling et al., 2009). The complete loss of FMRP leads to fragile X syndrome (FXS), the most common form of inherited intellectual disability and autism spectrum disorders (Willemsen et al., 2003; Bear et al., 2004; Bagni and Greenough, 2005). Point mutations

[1]Departamento de Ciencias Medicas Basicas-Fisiologia, Universidad de La Laguna, Tenerife, Spain; [2]Instituto de Tecnologías Biomedicas, Universidad de La Laguna, Tenerife, Spain; [3]Departamento de Biología, Facultad de Química y Biología, Universidad de Santiago de Chile, Santiago, Chile.

Correspondence to Teresa Giraldez: giraldez@ull.edu.es

This work is part of the special collection entitled "Electrical Signaling in the Heart and Nervous System: A Joint Meeting of the Society of General Physiologists and Latin American Society of Biophysicists."

(R138Q) or partial deletions in FMRP also lead to FXS (Bassell and Warren, 2008; Myrick et al., 2015). Besides FMRP's role in RNA regulation, several studies have shown that it directly interacts with presynaptic voltage-gated ion channels, regulating the gating of sodium-activated potassium channels (Slo2.2; Brown et al., 2010) and surface expression of N-type voltage-gated calcium channels ($Ca_V2.2$; Ferron et al., 2014). In addition, FMRP has been proposed to modulate BK channels in hippocampal and cortical excitatory neurons, regulating neurotransmitter release and synaptic transmission (Deng et al., 2013). Another study by the same group demonstrated that FMRP increases the open probability and modulates the gating kinetics of BKαβ_4 channels in CA3 pyramidal neurons (Deng and Klyachko, 2016). Interestingly, in that same work, the authors also showed that genetic up-regulation of BK channels through β_4 deletion was sufficient to normalize the neuronal defects in the FMRP knockout mice model. The modulation of BK channel function by FMRP has been proposed to occur through interaction with the accessory β_4 subunits, although the effect of FMRP on BKα-only channels was not directly addressed (Deng et al., 2013). A separate study including biochemical assays in whole mouse brain showed that FMRP could independently bind to both BKα and β_4 subunits (Myrick et al., 2015), hinting that BKα may be directly modulated by FMRP.

To better understand the regulation of BK channels by FMRP, we investigated its effects on the biophysical characteristics of BKα channels with or without β_4 accessory subunits in heterologous expression systems. Physical proximity between FMRP and BK channel components was addressed using super-resolution stochastic optical reconstruction microscopy (STORM). Our results demonstrate that FMRP interacts with and modulates the biophysical properties of BKα channels and, although to a lesser extent, BKαβ_4 channels. No effects were observed in the presence of the FMRP-R138Q mutant associated with intellectual disability and seizures, reinforcing the hypothesis of a direct link between BK channel dysregulation and FXS.

Materials and methods

Cell culture, transfection, cDNA constructs, and mutagenesis

HEK293T cells were cultured in Dulbecco's modified Eagle's medium containing 10% heat-inactivated FBS plus 1% penicillin/streptomycin and kept in a humidified incubator at 37°C, 5% CO_2. Cells were plated on 8-well glass-bottom micro-slides (Ibidi) for STORM experiments and on 12-mm polylysine-treated glass coverslips for electrophysiology experiments. Transfections were performed 24 h later with jetPrime reagent (Polyplus). The constructs used in this study were mammalian expression plasmids containing the human BKα (GenBank accession no. U11058), rabbit BKβ_4 (GenBank accession no. XM_002711330), and human FMRP (GenBank accession no. XM_002711330). Rabbit BKβ_4 shows 99% homology with the human BKβ_4 and has been shown to produce identical biophysical effects to the human homologue when coexpressed with BKα channels (Large et al., 2015). The R138Q mutation was introduced in the FMRP construct using the QuikChange site-directed mutagenesis kit (Agilent Genomics) and confirmed by sequencing.

Antibodies and immunostaining

Primary antibodies were mouse anti-BKα (ab192759; Abcam), rabbit anti-BKβ4 (ab222083; Abcam), and rat anti-HA (11867423001; Roche Applied Science). Secondary antibodies were goat anti-rat conjugated to Alexa Fluor 647 (ab150159; Abcam), goat anti-rabbit conjugated to Alexa Fluor 647 (A21245) or Alexa Fluor 488 (A11008), and goat anti-mouse conjugated to Alexa Fluor 647 (A32728) or Alexa Fluor 488 (A11001), all from Invitrogen. Cells at a density of 4×10^5 per well were fixed with 3% paraformaldehyde and 0.1% glutaraldehyde (Electron Microscopy Sciences, EM grade) in PBS for 10 min at room temperature and then reduced with 0.1% $NaBH_4$ in PBS for 7 min to mitigate cell auto-fluorescence. Next, cells were washed three times with PBS (5 min per wash) and then permeabilized with 0.2% Triton X-100 in PBS for 15 min. Subsequently, cells were blocked for 90 min with 10% normal goat serum and 0.05% Triton X-100 in PBS and incubated with primary antibodies for 1 h. Samples were washed five times with 1% normal goat serum and 0.05% Triton X-100 in PBS (10 min per wash), incubated with secondary antibodies for 1 h, and washed again. Cells were then fixed with 3% paraformaldehyde and 0.1% glutaraldehyde for 10 min, rinsed three times with PBS, and stored at 4°C until used.

STORM

STORM imaging was performed on a Nikon N-STORM super-resolution system with a Nikon Eclipse Ti inverted microscope equipped with an HP Apo TIRF 100× oil NA 1.49 objective (Nikon), a Perfect Focus System (Nikon), and an ORCA-Flash4.0 V2 Digital CMOS camera C11440 (Hamamatsu). Fluorescence emission was filtered with a 405/488/561/640-nm Laser Quad Band filter cube (TRF89901; Chroma). STORM imaging buffer contained 50 mM Tris-HCl (pH 8), 10 mM NaCl, 10% (wt/vol) glucose, 100 mM β-mercaptoethylamine, 0.56 mg/ml glucose oxidase, and 34 µg/ml catalase (all reagents from Sigma-Aldrich). Reconstructed images were generated from 5×10^4 acquired frames (2.5×10^4 per channel) using NIS-Elements software (Nikon). We performed at least three independent transfection experiments for each protein combination shown in this study. For every experiment, we determined the location of hundreds of thousands of molecules. Lateral localization accuracy was estimated, as described elsewhere (Shintani et al., 2005), as 13 ± 4 nm for Alexa Fluor 647 and 16 ± 6 nm for Alexa Fluor 488. Reconstructed images were filtered to remove background. Quantitative analysis of STORM images was performed using nearest-neighbor distance (NND) and cluster analysis using in-house script based on the density-based spatial clustering of applications with noise (DBSCAN) algorithm, similar to previously published work (Zhang et al., 2016; Fig. S1 and Supplemental text, see bottom of PDF). Comparable results were obtained by analyzing our data with a customized script using a distance-based clustering algorithm (Ricci et al., 2015; Zanacchi et al., 2017) kindly provided by Dr. Carlo Manzo (The Institute of Photonic Sciences, University of Vic, Barcelona, Spain).

Density filtering of 60-nm radius with a count of 10 molecules was found to fit best the clustering properties of the samples. Clusters were classified in three categories: "only red fluorophores," "only green fluorophores" (we refer to these two types as "homoclusters," formed by just one fluorophore), and "red and green fluorophores" (referred to as "heteroclusters," composed by more than one fluorophore). Cluster distributions are represented as plots of the percentage of each cluster type normalized to all clusters (all fluorophores).

Electrophysiology

Electrophysiological recordings were performed 24–48 h after transfection. Recordings were done using the patch-clamp inside-out configuration (Hamill et al., 1981) at room temperature (22–24°C), using an Axopatch-200B amplifier and Digidata 1550A plus HumSilencer system. Patch pipettes were fabricated from thick-wall borosilicate glass (1.5-mm OD × 0.86-mm inside diameter) using the Sutter P-97 puller and fire polished. The obtained pipettes had a resistance of 2–5 mΩ when filled with inside-out patch recording solutions, which contained (in mM) 80 $KMeSO_3$, 60 N-methylglucamine-$MeSO_3$, 20 HEPES, 2 KCl, and 2 $MgCl_2$ (pH 7.4). The bath solution contained (in mM) 80 $KMeSO_3$, 60 N-methylglucamine-$MeSO_3$, 20 HEPES, 2 KCl, 1 hydroxyethyl ethylenediamine triacetic acid, and $CaCl_2$ to give the desired free Ca^{2+} concentration. For whole cell recordings, the bath solution contained (in mM) 144 NaCl, 5.8 KCl, 0.9 $MgCl_2$, 2.1 $CaCl_2$, 0.1 NaH_2PO_4, 5.6 glucose, and 10 HEPES. The pipette solution contained (in mM) 135 KCl, 3.5 $MgCl_2$, 2 Na_2 ATP, 5 EGTA, and 5 HEPES, with pH adjusted to 7.4 with NaOH. To isolate the calcium currents, 135 $CsCl_2$ was used instead of KCl in the pipette solution and pH was adjusted to 7.4 with CsOH. The total amount of $CaCl_2$ needed to obtain the desired Ca^{2+} concentration was calculated using the Max Chelator program. Ca^{2+} concentrations were confirmed using a Ca^{2+}-sensitive electrode (Orion electrode; Thermo Laboratory Systems). Clampex and Clampfit software (pClamp10; Axon Instruments) were used for stimulus generation and data acquisition. Data were acquired at 100 kHz and low-pass filtered at 5 kHz with a four-pole Bessel filter.

Data analysis

G-V curves were generated from tail current amplitude data normalized to the maximum obtained in 100 µM Ca^{2+} and fitted with the Boltzmann equation (Eq. 1)

$$\frac{G}{G_{max}} = \frac{1}{1 + exp\left[\frac{(V_m - V_{\frac{1}{2}})}{z}\right]}, \quad (1)$$

where $V_{1/2}$ is the voltage of half-maximum activation, z is the slope of the curve, V_m is the test potential, and G_{max} is the maximal conductance.

We used the Horrigan–Aldrich (HA) allosteric model (Horrigan and Aldrich, 2002) to obtain information about the molecular mechanisms of BK channel modulation by FMRP. In this model, activation of the voltage and the Ca^{2+} sensors enables the opening of the channel (see Fig. 4, inset, Scheme I). These processes are defined by the three equilibrium constants, L, J, and K, related to the closed–open transition, voltage sensor activation, and Ca^{2+} binding, respectively. Additionally, the model includes three allosteric factors, D, E, and C, describing the coupling of the voltage sensor to channel opening, the interaction between the Ca^{2+} and voltage sensors, and the coupling of Ca^{2+} binding to channel opening, respectively (Horrigan and Aldrich, 2002). The open probability of the channel can be described by the following equation:

$$Po = \frac{1}{1 + \frac{(1+J+K+JKE)^4}{L(1+KC+JD+JKCDE)^4}}, \quad (2)$$

Our approach was to measure P_O under conditions where we could isolate the voltage dependence from Ca^{2+}-dependent gating. In the virtual absence of Ca^{2+}, the HA model can be simplified to Subscheme 1 (see Fig. 4, inset), which excludes the Ca^{2+}-dependent parameters. In this case, Eq. 2 is simplified to Eq. 3 below, where L defines the equilibrium of intrinsic gating, J is the equilibrium constant of voltage sensor activation, and D describes the allosteric coupling between them:

$$Po = \frac{1}{1 + \frac{(1+J)^4}{L(1+JD)^4}}. \quad (3)$$

The P_O was determined from the tail current amplitudes at −80 mV following depolarization pulses greater than +100 mV. The same patches were held at more negative potentials (+80 to −180 mV) for 5 s, and P_O was determined by single-channel analysis using a 50% amplitude threshold criterion in pClamp software. The number of channels in the patch was estimated by changing the perfusion from 0 to 100 µM Ca^{2+}. The voltage dependence of time constants of activation and deactivation at extreme negative voltages (Z_N) and at extreme positive potentials (Z_P) were obtained by fitting the data to the equation below, where τ_0 is the Tau value at 0 mV, and Z_X is either Z_N or Z_P:

$$\tau(V) = \tau_0 exp\left(\frac{Z_x.V}{KT}\right). \quad (4)$$

The equilibrium (L) of the gate to move between closed and open states can be determined by the equation

$$L = L_0 exp\left(\frac{Z_L.V}{k.T}\right), \quad (5)$$

where L_0 is the value of L at 0 mV, Z_L is the partial charge associated with the channel opening (C → O), and V, K, and T are same as above. The logarithmic slope of the P_O-V curve relationship gives the mean activation displacement Qa, which estimates the total charge movement upon channel opening (Sigg and Bezanilla, 1997; Webb et al., 2015). This is defined as (Eq. 6)

$$Q_a = kT\frac{d(ln(Po))}{dV}, \quad (6)$$

and was measured from the natural logarithm (ln) (P_O)-V relationship by linear regression (Ma et al., 2006). The P_O from individual experiments was converted to ln(P_O), and the gradient was determined over 60-mV intervals (approximately four

data points) across the entire range of membrane potentials. The mean Qa-V relationships were fitted with the following equation to generate the solid curves, as shown in Fig. 4 E:

$$Q_a \cong Z_L + 4Z_J\left\{\left[1+\left(\frac{1}{D}\right)e^{-(V-V_{HC})\frac{Z_J}{KT}}\right]^{-1} - \left[1+e^{-(V-V_{HC})\frac{Z_J}{KT}}\right]^{-1}\right\}. \quad (7)$$

Z_J represents the charge associated with the voltage sensor movement, while V_{HC} is the half-maximal activation of the voltage sensors when the channels are in the closed state. Statistical analysis was perfomed using one-way ANOVA for multiple comparisons with Bonferroni post hoc tests. In the text and figures, statistical significance is represented as *, $P < 0.05$; **, $P < 0.01$; and ***, $P < 0.001$.

Online supplemental material

Supplemental text appears at the bottom of the PDF and includes additional details about the quantitative analysis of the STORM data presented in the manuscript. Fig. S1 includes details about STORM analysis control. Table S1 lists the Boltzmann fit parameters of the G-V curves shown in Fig. 1, Fig. 5, and Fig. 7.

Results

FMRP associates with and modifies the gating characteristics of BKα channels

We investigated the effects of FMRP on pore-forming BKα channels in excised inside-out membrane patches from HEK cells coexpressing both proteins over a range of Ca^{2+} concentrations in the absence of any BK regulatory subunits. FMRP clearly altered activation and deactivation kinetics of BKα channels. For instance, at +100 mV, τ_{act} (activation time constant) increased twofold (from 3.1 ± 0.3 ms to 6.3 ± 0.5 ms; $P < 0.01$) and τ_{deact} (deactivation time constant) eightfold (from 0.3 ± 0.1 ms to 2.6 ± 0.2 ms; $P < 0.001$; Fig. 1 A). This effect was accompanied by a slight negative shift of $V_{1/2}$ values at all Ca^{2+} concentrations (Fig. 1, B and C; and Table S1; $P < 0.01$ in 0 µM Ca^{2+}). Using direct STORM (dSTORM) microscopy combined with TIRF, we examined the spatial distribution of FMRP and BKα channels (Fig. 1 D) at or near the plasma membrane. NND analysis revealed a bell-shaped distribution with a clear peak around 20–25 nm (Fig. 1 E), supporting the idea that BKα subunits and FMRP are in nanoscale proximity. Cluster analysis showed the presence of multi-protein complexes containing both BKα and FMRP at higher proportion than clusters composed exclusively by BKα or by FMRP (Fig. 1 F). This is in agreement with previous results showing coimmunoprecipitation of FMRP with BKα (Myrick et al., 2015). To discard the possibility of nonspecific assembly due to overexpression, we performed a control experiment using the δ subunit of the epithelial sodium channel (δENaC), which should not functionally (or physically) interact with BKα channels. Coexpression of BKα and δENaC yielded higher frequency of isolated green or red fluorescent signals that appeared to be at higher distances one from the other (Fig. 1 D). Consistent with this observation, image analysis revealed a broader NND distribution around lower peak values (Fig. 1 E) and a lower percentage of heteroclusters (Fig. 1 G).

Interestingly, the FMRP effect on the activation rate was observed not only in full BKα channels but also in BKα core constructs where the Ca^{2+} sensor domain (gating ring) had been completely removed (Budelli et al., 2013; Fig. 2; τ_{act} increased from 1.1 ± 0.2 ms to 6.4 ± 0.8 ms; $P < 0.001$). To test if the observed effect was accompanied by alteration in BKα surface expression levels, as has been proposed for $Ca_V2.2$ ion channels (Ferron et al., 2014), we compared the impact of FMRP coexpression on BKα current density levels with those of $Ca_V2.2$. Our results reproduced the 70% reduction of $Ca_V2.2$ current levels observed by Ferron et al. (2014), whereas the differences in BKα current density were significantly smaller (Fig. 3). This result suggests that FMRP directly regulates BKα channel activity, similar to what has been proposed with Slack ion channels (Brown et al., 2010).

All together, these results suggest that the observed effects of FMRP on the steady-state properties of BKα channels are due to direct interaction of these proteins and that FMRP actions may not be restricted to BK channels containing $BK\beta_4$ subunits.

Effects of FMRP on BKα gating

We aimed to identify the gating transitions associated with the observed kinetic changes induced by FMRP by using the allosteric modeling framework for BKα channels (Fig.4, inset, Scheme 1; Horrigan and Aldrich, 2002). Two observations prompted us to study the influence of FMRP on the parameters linked to the pore opening (L and Z_L) and voltage sensors (J, Z_J, and D) but not on the Ca^{2+} dependent parameters (C, E, and K). First, in spite of the clear effects on channel kinetics, the presence of FMRP did not dramatically affect Ca^{2+} sensitivity (Fig. 1 C). Second, the regulatory effects were still observed in BKα core channels (Fig. 2). Thus, we simplified the HA model into Subscheme 1 (Fig. 4, inset) and performed all the experiments in the virtual absence of Ca^{2+}.

The changes in the voltage dependence of C-O (Z_L) can be estimated by measuring the kinetics of the ionic K^+ currents (τ) at extreme voltages (Fig. 4 A). We did not observe differences in Z_L in the presence or absence of FMRP (Fig. 4 B), suggesting that the partial charges for channel opening (z_N and z_P) are not altered by FMRP. Subsequently, we obtained the P_O-V relationships over a wide range of voltages and determined the values of the gating parameters according to the HA model (Horrigan and Aldrich, 2002). These data with their corresponding fits are presented in Fig. 4, C and D and summarized in Table 1. The FMRP-induced negative shifts in the P_O-V relationships can be explained by a twofold increase in L_0 and a 3.5-fold increase in voltage sensor activation (J_0). The increase in L_0 related to intrinsic gating (i.e., independent of Ca^{2+} or voltage sensor activation) is consistent with the single-channel data from BKα+FMRP–excised membrane patches showing an increased P_O at very negative voltage values compared with patches containing only BKα channels (Fig. 4 C). Alterations of the gating charge parameter Z_J or the allosteric constant D were not compatible with the data (Table 1). FMRP induced a negative shift in the V_{HC} (approximately −50 mV) of BKα channels, in agreement with the idea that it shifts the voltage-sensor equilibrium toward negative potentials (Table 1). These results are consistent with

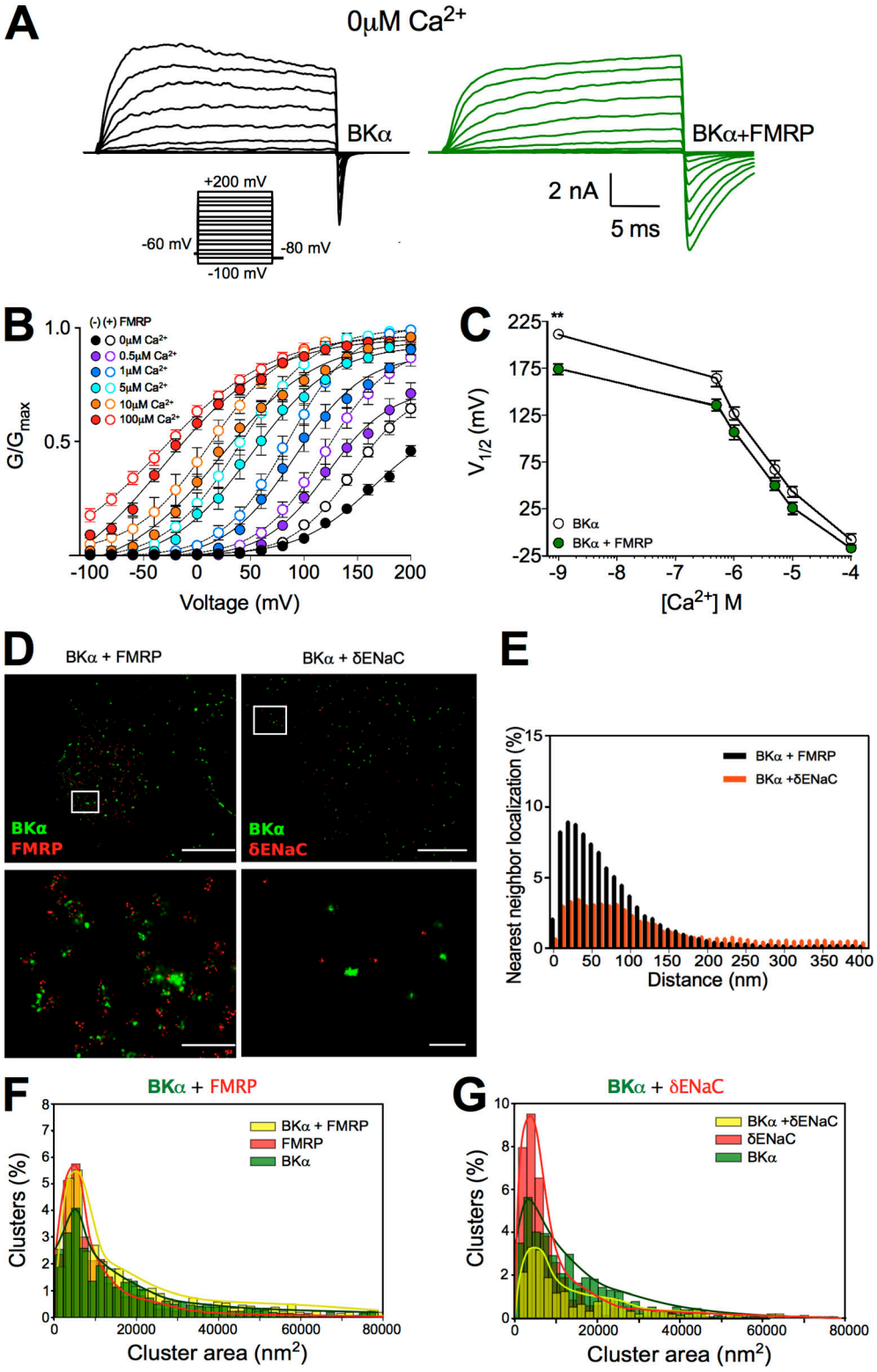

Figure 1. **FMRP is localized in nanoscale proximity to BKα channels and alters their gating properties. (A)** Representative BKα current recordings from inside-out patches at 0 μM Ca^{2+} in the absence (black traces) and presence (green traces) of FMRP, after applying the voltage protocol shown in the inset (−100 mV to +200 mV in 20-mV increments). **(B)** G-V curves obtained at various Ca^{2+} concentrations, color-coded as indicated in the graph legend. Empty symbols correspond to cells expressing BKα and full-colored symbols to BKα+FMRP. Solid lines represent Boltzmann fits to the data. **(C)** Mean $V_{1/2}$ values plotted as a function of Ca^{2+} concentration. Error bars represent SEM. **(D)** Representative dSTORM images (top) and magnified views of areas of interest (bottom) showing the spatial distribution of BKα (green, Alexa Fluor 488) with either FMRP (left panels, red, Alexa Fluor 647) or δENaC (right panels, red, Alexa Fluor 647) proteins. Scale bars represent 5 μm (top) and 0.5 μm (bottom). **(E)** NND analysis from the corresponding dual-label experiments. **(F and G)** Histograms representing the distribution of clusters containing BKα alone (green bars), FMRP alone (red bars in F) or δENaC alone (red bars in G), and both proteins (yellow bars). Colored curves outline the histograms to facilitate visualization. **(F)** n = 25 cells from three different transfection experiments, 2,591 clusters. **(G)** n = 7 cells, 1,549 clusters). **, $P < 0.01$.

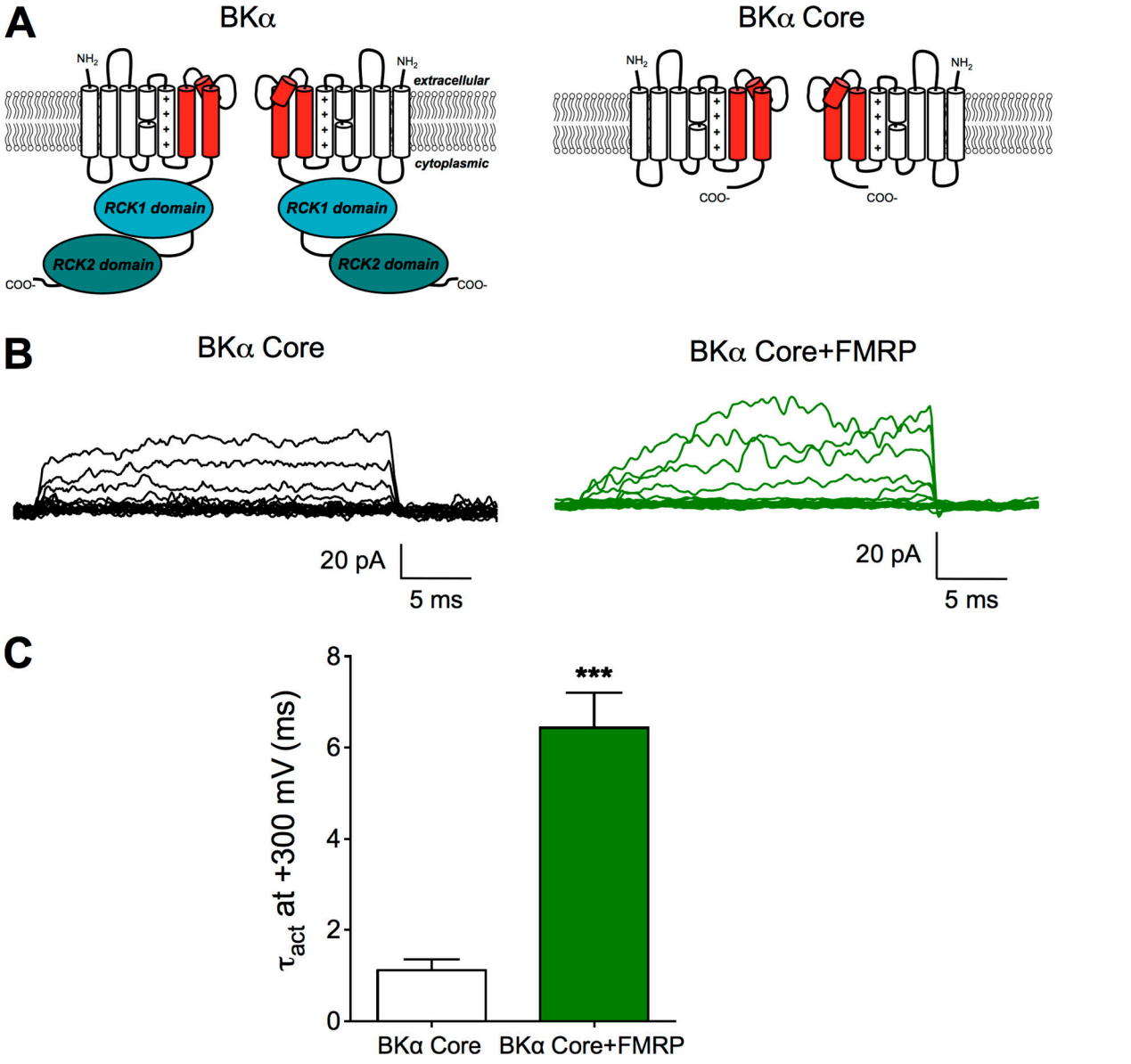

Figure 2. **The Ca^{2+} sensor (gating ring) is not required for FMRP modulation of BKα channels. (A)** Cartoon depicting the structures of BKα and BKα core channel subunits. The BKα core channels lack the entire cytoplasmic domain containing two RCK domains. **(B)** Representative current traces from patches expressing BKα core channels in the absence (black traces) and presence of FMRP (green traces) in 0 μM Ca^{2+}. These patches were stepped from −100 to +300 mV in 20-mV steps. FMRP clearly altered the activation kinetics of BKα core channels. **(C)** τ_{act} measured in response to a depolarizing step at +300 mV. ***, P < 0.001. Error bars represent SEM.

the Q_a-V plots shown in Fig. 4 E, which were calculated from the logarithmic slope of the P_O-V data and fitted with Eq. 7 (Table 2). Therefore, our results suggest that in the absence of β_4 subunits, FMRP interacts with BKα channels, favoring activation by simultaneously decreasing the energy needed for channel opening and shifting the activation of voltage sensors toward more negative voltages.

FMRP associates with BKαβ_4 channels and only modestly alters their biophysical properties

We next evaluated the effect of FMRP on BKαβ_4 channels using the same experimental setup. In agreement with previous studies (Behrens et al., 2000; Brenner et al., 2000; Orio et al., 2002; Wang et al., 2006), coexpression of BKβ_4 with BKα subunits slowed down channel deactivation (Fig. 5 A) and shifted the $V_{1/2}$ toward negative values at Ca^{2+} concentrations >10 μM (Fig. 5, B and C). Contrary to what was expected, coexpression of FMRP with BKαβ_4 channels did not result in dramatic functional differences. We did observe moderate effects in the voltage dependence of activation, which was shifted to more negative values compared with BKαβ_4 channels (Fig. 5, B and C; P < 0.05 in 0 μM and 1 μM Ca^{2+}). Additionally, FMRP slowed down (about twofold) the BKαβ_4 gating kinetics at potentials below +80 mV (Fig. 5 D). The τ-V relationships reflected the decrease in activation and deactivation rates in BKαβ_4 channels versus BKα channels (Fig. 5 D). However, coexpression with FMRP revealed

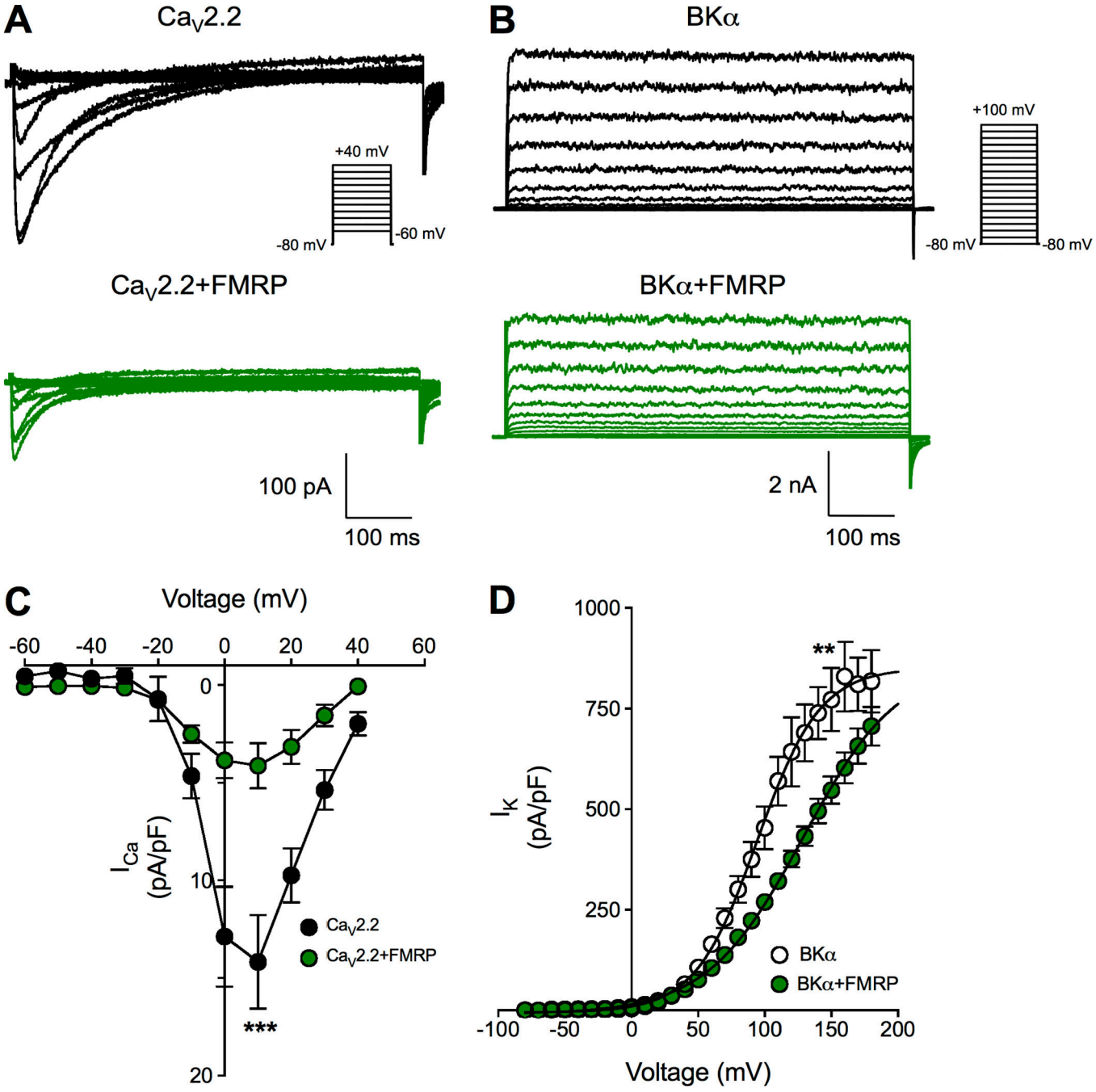

Figure 3. **Effects of FMRP on $Ca_V2.2$ and BK channels current density. (A and B)** Representative whole-cell current recordings from cells transfected with either $Ca_V2.2/\alpha_2\delta_1/\beta_3$ channels (A) or BKα channels (B) in the absence (top, black traces) and presence of FMRP (bottom, green traces), respectively. The voltage commands are shown in the insets. **(C and D)** Average current-voltage relationships obtained with $Ca_V2.2/\alpha_2\delta_1/\beta_3$ channels (C) or BKα channels (D). Coexpression of FMRP results in a 70% reduction of $Ca_V2.2$ channel current density (I_{Ca}; at +10 mV, peak $Ca_V2.2$ current density = 14.1 ± 2 pA/pF, n = 5; $Ca_V2.2$+FMRP current density = 4.1 ± 1 pA/pF, n = 5). In contrast, BKα channel current density (I_K) is only reduced ~30% in the presence of FMRP (at +160 mV, peak BKα current density = 829 ± 86 pA/pF, n = 9; BKα+FMRP current density = 603 ± 38 pA/pF, n = 8). **, P < 0.01; ***, P < 0.001. Error bars represent SEM.

no further effects other than the above-mentioned slight increase in the deactivation time constants. The fold change in the time constant was quantitatively similar in 0 µM and 1 µM Ca^{2+}. Specifically, coexpression with FMRP increased the τ_{deact} of BKαβ_4 channels (at +100 mV, 0 µM Ca^{2+}) from 1.0 ± 0.1 ms to 1.6 ± 0.1 ms (~1.6-fold increase, absence versus presence of FMRP). Similarly, in 1 µM Ca^{2+}, the observed change of τ_{deact} was from 2.7 ± 0.2 ms to 5.2 ± 0.2 ms (~1.9 fold). The P_O-V relationships in the presence of FMRP showed an increase in open probability (Fig. 5 E) and a shift toward negative voltages, although the change was moderate compared with the effect on BKα alone (Fig. 5 F). Fits to the HA allosteric model revealed a ninefold change in the intrinsic gating parameter L_0 (BKαβ_4 9.8 × 10^{-7}; BKαβ_4+FMRP 8.6 × 10^{-6}; Table 1) without significant changes in

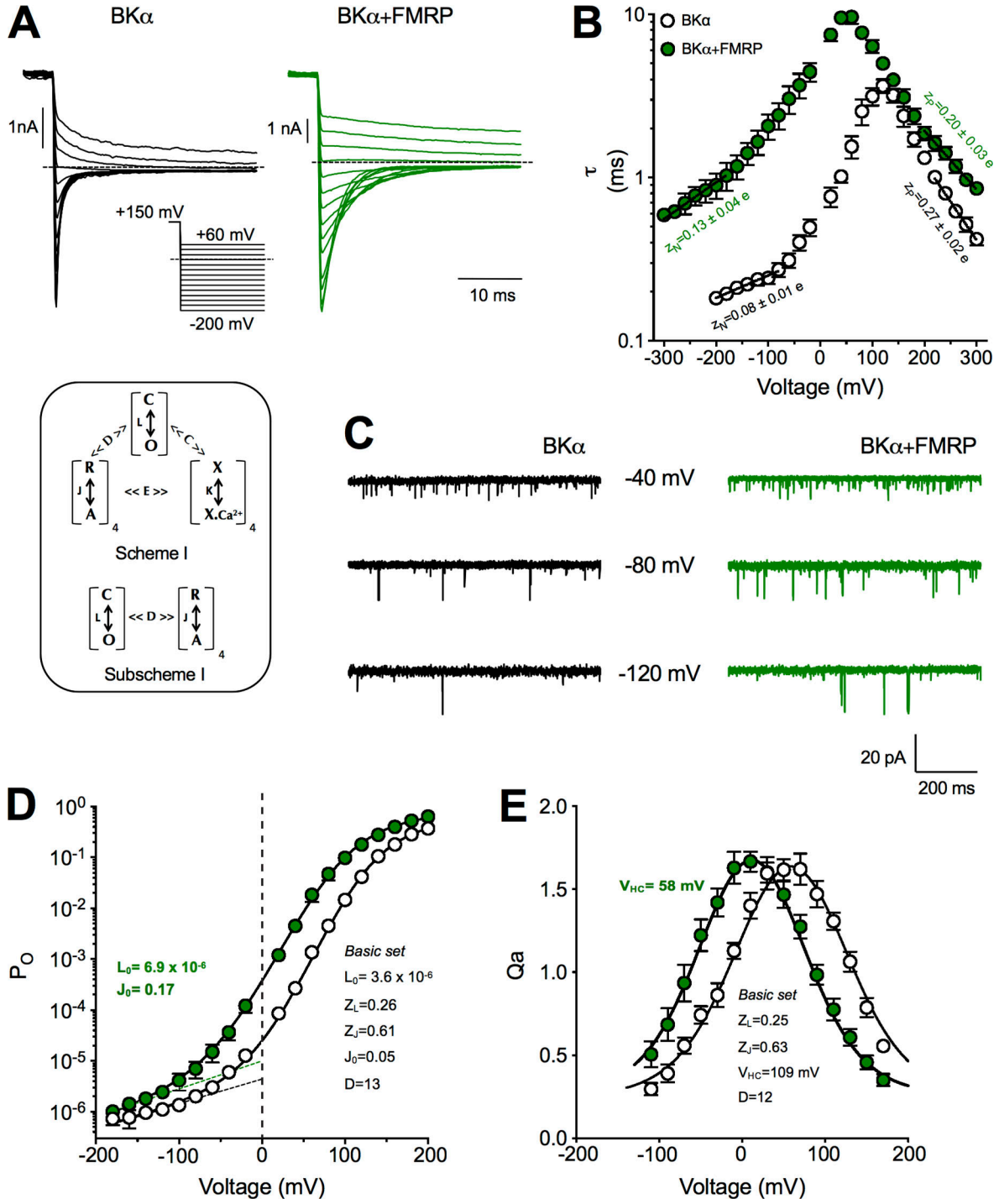

Figure 4. **FMRP modulates parameters associated with voltage sensor activation (J_0) and channel opening (L_0). (A and B)** Schematic of the HA allosteric gating model (inset, Scheme I). The three processes of voltage sensor activation (R ↔ A), calcium binding (X ↔ X_{Ca}^{2+}), and pore opening (C ↔ O) are governed by equilibrium constants J, K, and L, respectively. The allosteric factors C, D, and E couple the three events. Simplification of the HA model in the absence of Ca^{2+} (inset, Subscheme I). Comparison of deactivation kinetics (A) and mean τ-V relationships (B) between BKα and BKα+FMRP channels in 0 µM Ca^{2+}. The voltage protocols used for measuring τ_{deact} are also shown below. The solid lines show exponential fits to the data for five extreme negative and positive voltages with Eq. 4. **(C)** Single-channel recordings from BKα channels (black traces) and BKα+FMRP channels (green traces) at −40, −80, and −120 mV in the absence of Ca^{2+}. The BKα patch contained 190 channels and the BKα+FMRP patch contained 170 channels approximately. Note the increased P_O values inBKα+FMRP–expressing patches at all the voltages tested. **(D)** Mean P_O-V relationships in the absence (clear circles) and presence of FMRP (green circles) in log scales. Solid lines are fits with Eq. 3, which yielded the basic set values in BKα alone (see Table 1). The presence of FMRP increased the equilibrium constants for pore opening (L_0) and voltage sensor activation (J_0). **(E)** Mean Q_a-V relationships between BKα and BKα+FMRP channels. Solid lines are fits with Eq. 7, which yielded the basic set values in BKα alone (see Table 2). Error bars represent SEM.

Table 1. **Best fit parameters for P_o-V data with the HA model**

Parameter	BKα	+FMRP	BKαβ$_4$	+FMRP
L_0	3.6 × 10^{-6}	6.9 × 10^{-6}	9.8 × 10^{-7}	8.6 × 10^{-6}
Z_L	0.26	0.29	0.23	0.27
J_0	0.05	0.17	0.12	0.15
Z_J	0.61	0.58	0.59	0.55
D	13	13	16	11
$V_{HC,\ mV}$	124	77	91	87
$V_{HO,\ mV}$	18	−35	−28	−23

Best fit values for P_O-V data from Fig. 4 D and Fig. 5 F with Eq. 3. Z_L and L_0 values were determined from Eq. 5 and were constrained to yield the values shown. Columns 2 and 4 correspond to the indicated subunit combinations in the absence of FMRP. Columns 3 and 5 correspond to the indicated subunit combinations in the presence of FMRP (0 µM Ca^{2+}).

Table 2. **Best fit parameters for Q_a-V data with the HA model**

Parameter	BKα	+FMRP	BKαβ$_4$	+FMRP
Z_L	0.25	0.26	0.24	0.25
Z_J	0.63	0.66	0.6	0.66
D	12	11	13	9
$V_{HC,\ mV}$	109	58	81	65

Best fit values for Q_a-V data in Fig. 4 E and Fig. 5 G using Eq. 7. Columns 2 and 4 correspond to the indicated subunit combinations in the absence of FMRP. Columns 3 and 5 correspond to the indicated subunit combinations in the presence of FMRP (0 µM Ca^{2+}).

J_0 (BKαβ$_4$ 0.12; BKαβ$_4$+FMRP 0.15; Table 1). Consistent with these findings, FMRP failed to shift the Q_a-V relationships of BKαβ$_4$ channels more negatively than that of BKα alone (ΔV_{HC} approximately −15 mV, Table 2; compare Fig. 5 G with Fig. 4 E). These results indicate that the effects of FMRP on BKαβ$_4$ channels are more complex than initially envisioned. In any case, the presence of FMRP seems not to abrogate the regulation of BKα by BKβ$_4$ subunits, but rather to slightly potentiate it.

Is this functional effect due to association of FMRP with BKαβ$_4$ channels? We addressed this question using super-resolution microscopy to study the spatial organization of BKα channels, BKβ$_4$ subunits, and FMRP. Our experimental approach only allows us to perform dual labeling (see Materials and methods). Therefore, we imaged all possible combinations of labeled pairs to puzzle out the contribution of complexes containing different combinations of the three proteins. Close localizations of BKα-FMRP, BKβ$_4$-FMRP, and BKα-BKβ$_4$ were observed (Fig. 6 A). This is reflected in the NND distribution analysis, showing a higher peak at 25–30 nm for all the combinations (Fig. 6 B). Our results show a similar fraction of BKα-FMRP associations in the presence of BKβ$_4$ (compare Fig. 1 F and Fig. 6 C). More importantly, the NND distribution and the relative fraction of BKα-BKβ$_4$ complexes remained unaltered in the presence of FMRP (compare Fig. 6 B with Fig. 8 B, and Fig. 6 D with Fig. 8 C). Many uncertainties, including the lack of an accurate description of the physiological BKα:BKβ$_4$ stoichiometries (Gonzalez-Perez and Lingle, 2019), prevent us from elaborating a quantitative model of interaction. All the same, this finding suggests that when BKα is expressed with BKβ$_4$ and FMRP, all three proteins are located together with high probability. This argues against the possibility that FMRP and BKβ$_4$ interact with BKα in a mutually exclusive way.

The disease-related FMRP-R138Q mutant shows no functional effects on BK channels

The missense mutation R138Q in the *FMR1* gene associates with intellectual disability and seizures (Myrick et al., 2015). This mutation results in a partial loss-of-function of FMRP, which maintains its ability to regulate translation but lacks presynaptic effects. Myrick et al. (2015) hypothesized that the resulting FMRP$^{(R138Q)}$ protein resulted in impaired interactions with BK channels in mice central neurons. In this study, we examined the functional effects of the mutant FMRP$^{(R138Q)}$ on BKα and BKαβ$_4$ channels. Our prediction was that this nonfunctional FMRP mutant would not exert any of the previously observed effects on the channel kinetics, which would also be reflected in lower levels of protein associations. Fig. 7 A shows the effect of FMRP$^{(R138Q)}$ on BKα channels. The mutant did not modify BKα gating characteristics (at +100 mV, τ_{act} = 3.1 ± 0.3 ms for BKα channels versus 3.7 ± 0.5 ms for BKα+FMRP$^{(R138Q)}$ channels; P = 0.40). Similarly, FMRP$^{(R138Q)}$ also failed to alter the steady-state parameters when coexpressed with BKαβ$_4$ channels (Fig. 7 B). These results are in agreement with previous results (Myrick et al., 2015) suggesting that the FMRP$^{(R138Q)}$ construct shows impaired interaction with BK channels in heterologous systems.

Using STORM, we examined how coexpression of FMRP$^{(R138Q)}$ affected the spatial distribution of BKα or BKα-BKβ$_4$ protein complexes. Similar to wild-type FMRP, FMRP$^{(R138Q)}$ localized at nanoscale distances from BKα (Fig. 7 C, left panels) in the absence of BKβ$_4$. This was reflected in the NND analysis distribution, showing a peak around 20 nm (Fig. 7 D). The cluster analysis indicated the presence of complexes formed by BKα and FMRP$^{(R138Q)}$, which seemed to occur at higher levels than BKα-only channels but less frequently than protein complexes containing exclusively FMRP$^{(R138Q)}$ (Fig. 7 E). BKα and BKβ$_4$ in the presence of FMRP$^{(R138Q)}$ also exhibited close localizations with around 50% of the NND distances within the 0–50 nm range (Fig. 7 D). Cluster analysis of the STORM data from cells expressing BKα-BKβ$_4$-FMRP$^{(R138Q)}$ showed a lower incidence of multimeric clusters containing BKα+BKβ$_4$ compared with coexpression of BKα+BKβ$_4$ with wild-type FMRP (compare yellow bars in Fig. 7 F with Fig. 6 D). Previously published observations suggested that the R138Q mutation in FMRP altered its association with BKβ$_4$ (Myrick et al., 2015). Consistent with this notion, super-resolution data in cells expressing BKα-BKβ$_4$-FMRP$^{(R138Q)}$ showed a broader distribution of lower BKβ$_4$-FMRP$^{(R138Q)}$ NND values (Fig. 8 B) and a reduced fraction of BKβ$_4$-FMRP$^{(R138Q)}$ complexes (Fig. 8 D).

Discussion

In spite of the recent advances in uncovering the novel roles of FMRP in ion channel modulation (Brown et al., 2010; Deng et al., 2013; Ferron et al., 2014), important questions remain about the

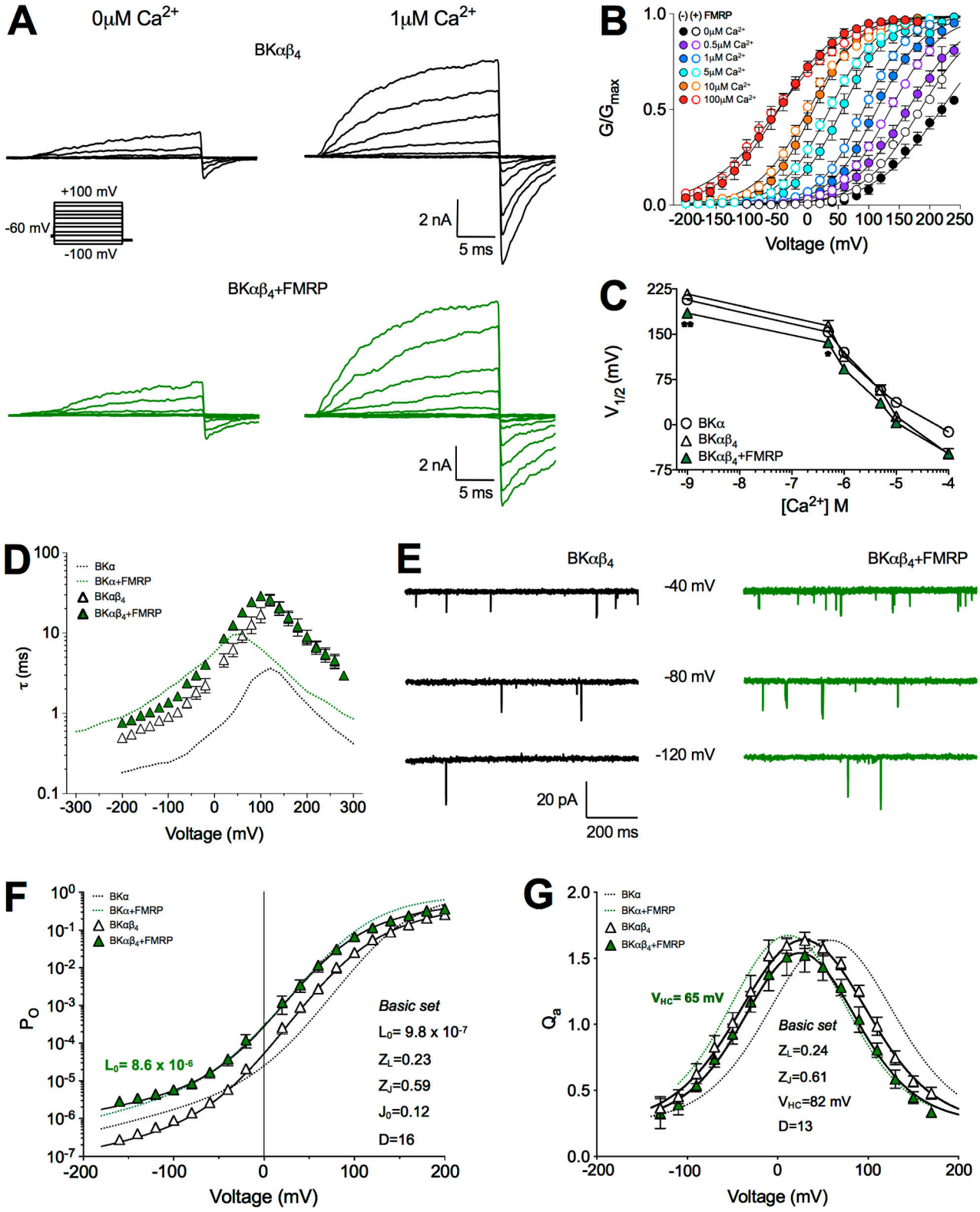

Figure 5. **FMRP effects on BKαβ$_4$ channels. (A)** Representative current recordings from BKαβ$_4$ channels in the absence (black traces) and presence of FMRP (green traces) in 0 μM and 1 μM Ca^{2+} after applying a family of voltage steps from −100 to +100 mV in 20-mV increments (inset below). **(B–D)** Average G-V relationships (B), $V_{1/2}$ versus Ca^{2+} concentration plots (C), and mean τ-V relationships (D) in the absence (white triangles) and in the presence of FMRP (green triangles). **(E)** Typical records of single-channel currents from patches expressing BKαβ$_4$ (left) and BKαβ$_4$+FMRP channels (right) held at −40, −80, and −120 mV in the absence of Ca^{2+}. The BKαβ$_4$ and BKαβ$_4$+FMRP patches contained ∼210 channels and 195 channels, respectively. **(F and G)** Mean P_O-V (F) and Q_a-V (G) relationships for BKαβ$_4$ channels in the absence (white triangles) and in the presence (green triangles) of FMRP. Solid curves in F and G represent fits to the data using Eq.3 and Eq. 7, respectively, to yield the basic set values shown. For reference, values corresponding to BKα (±FMRP) channels (Fig. 4) are represented as dotted lines. *, P < 0.05; **, P < 0.01. Error bars represent SEM.

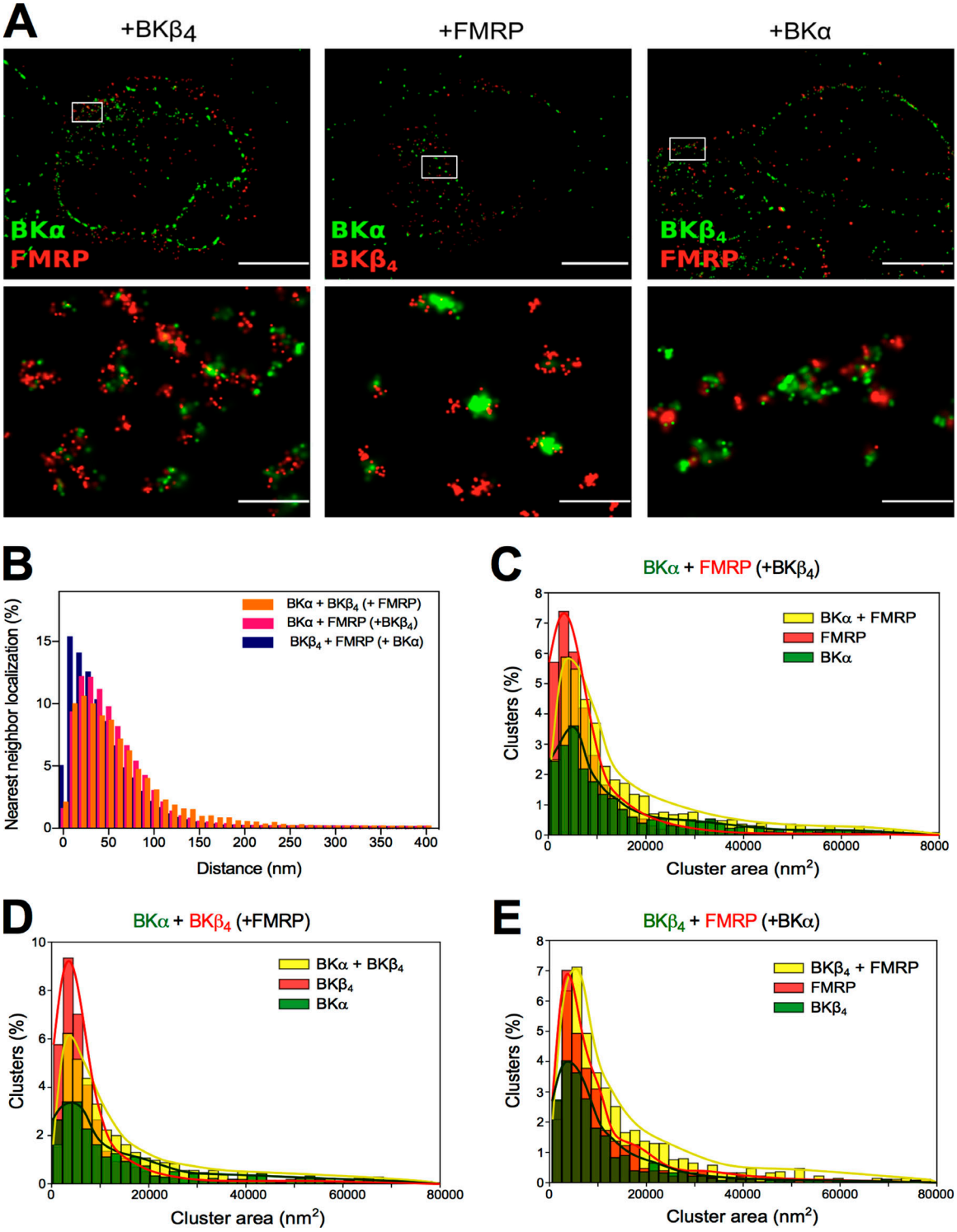

Figure 6. **BKαβ4 complexes are located in close proximity to FMRP. (A)** Representative dSTORM full images (top) and magnifications (bottom) showing areas of clusters constituted by BKα (green)-FMRP (red) in the presence of BKβ4 (left panels), BKα (green)-BKβ4 (red) in the presence of FMRP (middle panels), and BKβ4 (green)-FMRP (red) in the presence of BKα (right panels). Scale bars represent 5 µm (top panels) and 0.5 µm (bottom panels). **(B)** NND analysis corresponding to the experiments above. Color labels correspond to dual labeling BKα-FMRP (with unlabeled BKβ4; pink bars), BKα-BKβ4 (with unlabeled FMRP; orange bars), and BKβ4-FMRP (with unlabeled BKα; blue bars). **(C–E)** Histograms represent the distribution of cluster areas of protein complexes in each of the three experiments above. The color code corresponds to clusters containing either of the two labeled proteins alone (red or green bars) or both labeled proteins (yellow bars) in the presence of the unlabeled third protein (C, *n* = 24 cells, 3,576 clusters; D, *n* = 15 cells, 2,153 clusters; E, *n* = 20 cells, 2,781 clusters).

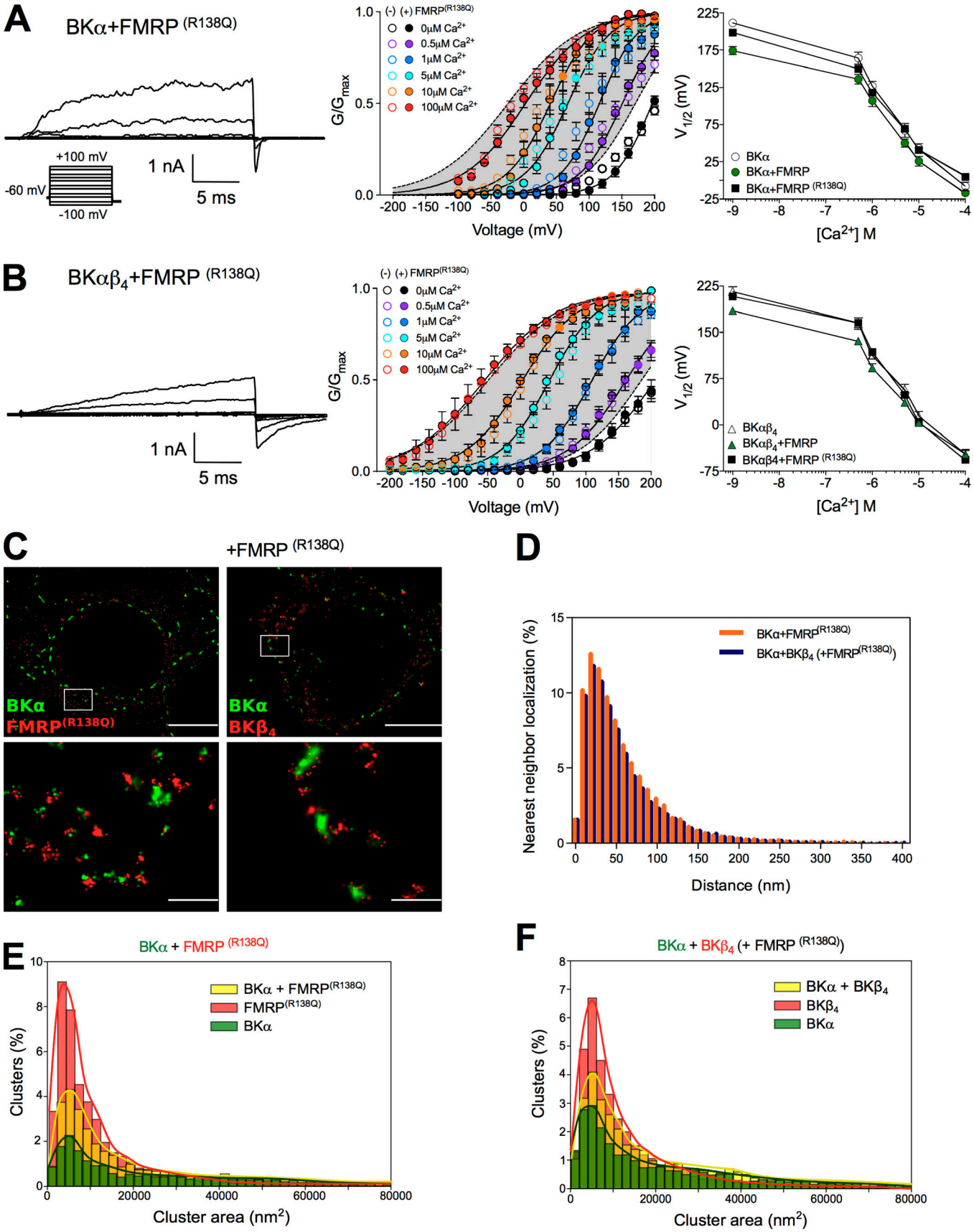

Figure 7. **FMRP$^{(R138Q)}$ mutant preserved the physical coupling between BKα and BKβ$_4$ proteins, but it failed to produce an effect on BKα and BKαβ$_4$ channel kinetics. (A and B)** Representative current recordings from –100 to +100 mV (left), summary G-V relations (middle), and mean $V_{1/2}$ versus Ca^{2+} plots

(right) for BKα (A) and BKαβ$_4$ (B) channels coexpressed with FMRP$^{(R138Q)}$. Empty symbols correspond to cells expressing either BKα or BKαβ$_4$, and full-colored symbols correspond to either BKα+FMRP$^{(R138Q)}$ or BKαβ$_4$+FMRP$^{(R138Q)}$. Gray shadows indicate the full range of G-V curves from 0 µM to 100 µM Ca^{2+} of BKα+FMRP (Fig. 1 B) and BKαβ$_4$+FMRP (Fig. 5 B) channels. Error bars represent SEM. **(C)** Representative dSTORM images (top) and corresponding magnifications of areas (bottom) containing clusters in different labeling conditions. Left panels: BKα (green) and FMRP$^{(R138Q)}$ (red). Right panels: BKα (green) and BKβ$_4$ (red) in the presence of FMRP$^{(R138Q)}$. Scale bars represent 5 µm (top panels) and 0.5 µm (bottom panels). **(D)** NND analysis for the combination BKα-FMRP$^{(R138Q)}$ (orange bars) or BKα-BKβ$_4$ in the presence of FMRP$^{(R138Q)}$ (blue bars). **(E and F)** Histograms represent the distribution of cluster areas for the protein complexes constituted by either of the two proteins alone (red or green bars) or by both proteins forming part of the same cluster (yellow bars) in the presence of the unlabeled third protein (E, *n* = 17 cells, 10,615 clusters; F, *n* = 17 cells, 10,390 clusters).

underlying molecular mechanisms. FMRP is a ubiquitous protein with a growing number of proposed functions (Ferron, 2016). BK channels can be expressed in a large variety of cells and tissues, with or without regulatory subunits from the BKβ and BKγ families (Latorre et al., 2017). In this study, we have tested the effects of FMRP on BK channels containing different subunit combinations of physiological relevance in neurons using a heterologous expression system. Using electrophysiological measurements, we have addressed the effects of FMRP on BK channel biophysical properties. These functional data have been correlated with the relative localization of the proteins using super-resolution microscopy.

One of our most relevant findings reveals that in the absence of regulatory subunits, FMRP has a clear effect on BKα channel

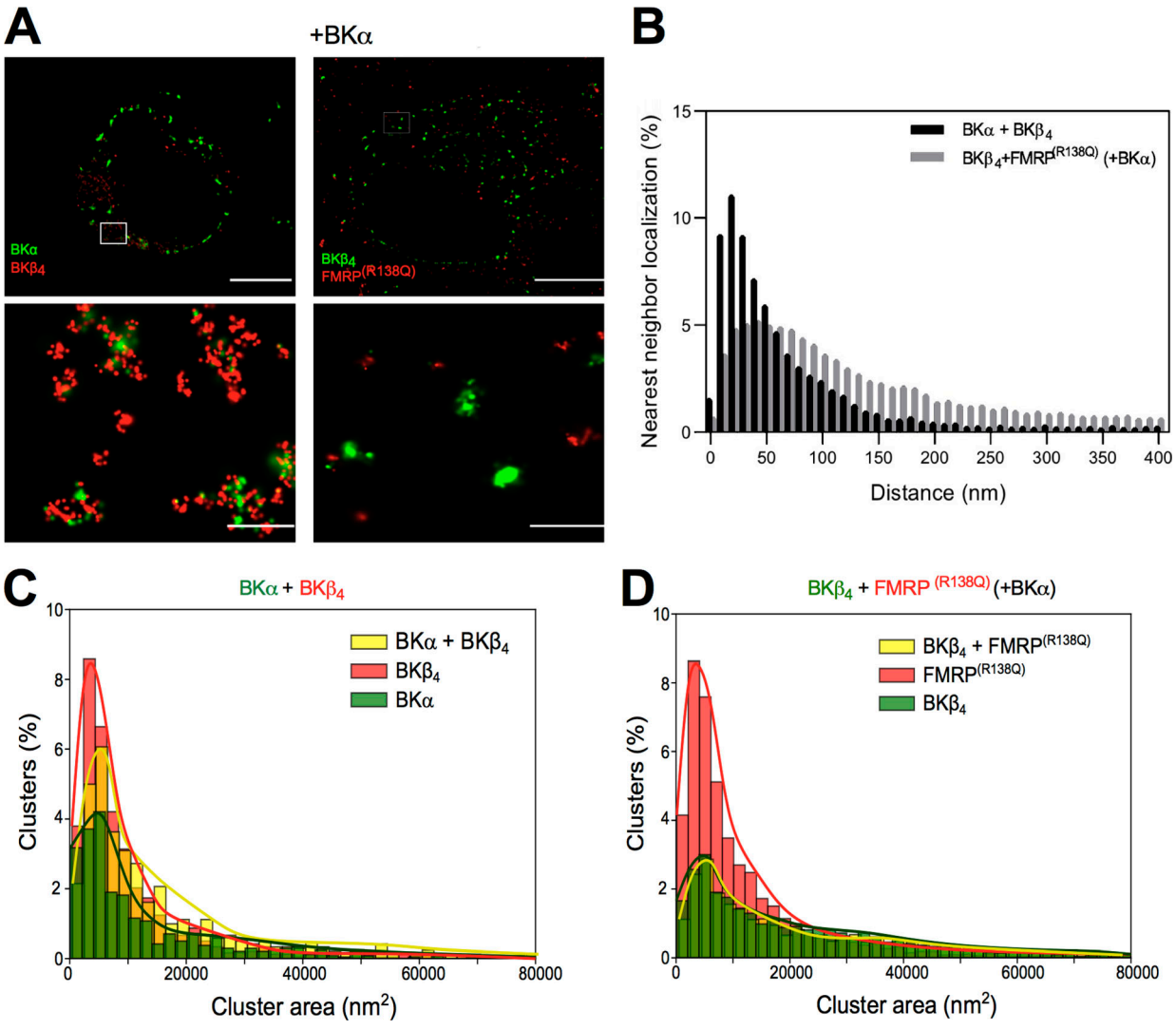

Figure 8. **FMRP$^{(R138Q)}$ mutation markedly reduced the associations between BKβ$_4$ and FMRP. (A)** Representative dSTORM images and corresponding magnified areas showing clusters constituted by BKα (green)-BKβ$_4$ (red; left panels) and BKβ$_4$ (green)-FMRP $^{(R138Q)}$ (red) in the presence of BKα (right panels). Scale bars represent 5 µm (top panels) and 0.5 µm (bottom panels). **(B)** NND analysis of experiments in panel A. **(C and D)** Histograms show the distribution of cluster areas corresponding to protein complexes, including either of the two proteins alone (red or green bars) or both proteins (yellow bars), in the presence of the unlabeled third protein (BKα) in D (C, *n* = 18 cells, 2,424 clusters; D, *n* = 19 cells, 10,938 clusters).

kinetics, mostly consisting of an eightfold increase in the current deactivation time constants. The P_O-V relationship is shifted toward more negative values, which can be explained in the context of the BK allosteric model (Horrigan and Aldrich, 2002) by decreasing the energetic barrier for the C-O transition (twofold increase in constant L_0) and/or shifting the activation of the voltage sensors toward more negative voltages (3.5-fold increase in J_0). The first explanation is consistent with the observation that in the presence of FMRP, higher P_O of BKα channels is observed at very negative voltages (when both the Ca^{2+} and voltage sensor are not activated). The latter explanation is supported by the hyperpolarization shift (−50 mV) noted in the Q_a-V relationship in the presence of FMRP. This finding requires further confirmation by gating current recordings to assess directly the impact of FMRP on the voltage sensor function.

Several lines of evidence indicate that this regulatory effect occurs via close interaction of both proteins. First, the FMRP effects are observed in isolated inside-out patches. Second, STORM data show close localization of both proteins in the nanoscale range (NND distribution peak around 20 nm) and high occurrence of BKα+FMRP protein clusters. The interaction may possibly occur at the transmembrane region or the S6/RCK1 linker, since part of the regulatory effects of FMRP on the channel are preserved in BKα channels where the intracellular Ca^{2+} sensor has been completely truncated. Finally, we provide further evidence showing that coexpression of FMRP with BKα does not have a strong impact on current density levels, as opposed to the FMRP-regulated $Ca_V2.2$ channel membrane abundance via proteasome-mediated degradation (Ferron et al., 2014). Altogether, our results are in agreement with the proposed translation-independent regulatory mechanisms of Slo2.2 and BKαβ_4 channels by FMRP (Brown et al., 2010; Deng et al., 2013).

We compared the effects of FMRP on BKα channels with those on BKαβ_4 channels. The complex effects of the BKβ_4 subunit on BKα gating were previously explained in the context of the HA allosteric model by a decrease in the L_0 constant (closed-to-open transition) and a decrease in V_{HC} (favoring voltage sensor activation; Wang et al., 2006). An alternative model has been proposed where the effects of the BKβ_4 subunits are explained by the stabilization of the voltage sensor in the active conformation and a reduction in the number of gating charges per sensor (Contreras et al., 2012). Our experiments qualitatively reproduced these effects. Coexpression of BKα with BKβ_4 caused a decrease in the L_0 constant, a negative shift in V_{HO} (half-maximal activation of the voltage sensors when the channels are in the open state), and an increase in J_0 values. According to the hypothesis proposed by Deng et al. (2013), we were expecting that in the presence of FMRP the effect of the BKβ_4 subunits would be abrogated. However, this was not the case. Rather than reversing the BKβ_4 effects, FMRP seemed to slightly potentiate them. The shift in the P_O-V curve toward more negative voltages was consistent with higher τ values at negative voltages. In the context of the HA allosteric model, this effect could be explained by increased intrinsic gating (ninefold increase in L_0), while other parameters remained very similar to BKαβ_4 channels. STORM experiments showed a high incidence of heteroclusters containing the three proteins, confirming the association of FMRP to complexes containing BKα and BKβ_4 subunits. Altogether, these data support the previously proposed hypothesis that FMRP binds to BKαβ_4 channels in CA3 neurons, regulating their function by increasing P_O (Deng et al., 2013; Deng and Klyachko, 2016). Further work is needed to understand the mechanisms underlying homo- and heterocluster formation, as well as the possible participation of other proteins in these complexes.

All the observed effects of FMRP on BKα and BKαβ_4 channels were greatly reduced by introducing the R138Q mutation in the FMRP protein. This missense mutation was described to disrupt the regulatory role of FMRP in AP duration, presumably by perturbation of its ability to interact with BK channels, while not altering other canonical roles involving RNA binding and regulation of translation (Myrick et al., 2015). One possible explanation for the lack of regulatory effects by $FMRP^{(R138Q)}$ in our experiments could be that this mutation is associated with reduced expression levels. However, this possibility is ruled out by the results in the STORM experiments showing similar expression levels of $FMRP^{(R138Q)}$ than wild-type FMRP. Instead, the observed lack of regulatory effects of the $FMRP^{(R138Q)}$ mutant on BKαβ_4 channels seem to be due at least partly to weaker interactions of $FMRP^{(R138Q)}$ with BKβ_4. These results are in agreement with previous data showing impaired (but not fully abolished) $FMRP^{(R138Q)}$-BKβ_4 interactions (Myrick et al., 2015).

A possible explanation for the findings of our study is summarized in the cartoon depicted in Fig. 9. Our data show that FMRP locates closely to BKα subunits and modulates their function, resulting in increased channel P_O at physiological voltage values (Fig. 9 A). In the presence of BKβ_4 subunits, FMRP associates with complexes containing both BKα and BKβ_4 subunits to regulate their function, slightly potentiating the effects of BKβ_4 regulation (Fig. 9 B). The biophysical properties of BKαβ_4 channels in the presence of FMRP are not equivalent to BKα-only channels, implying the existence of a more complex mechanism other than the sequestration of BKβ_4 subunits, as previously described (Deng et al., 2013). It is important to note that our model cannot rule out the participation of other proteins in the functional complexes. The most relevant conclusion of our data is that, depending on the physiological context, FMRP may regulate BK currents via modulation of BKα and/or BKαβ_4 channels.

Physiological relevance

In central neurons, contribution of type II BK channels (formed by BKαβ_4 complexes) to electrical activity depends on the local intracellular Ca^{2+} concentrations. At low Ca^{2+} concentrations (i.e., <10 µM Ca^{2+}), it has been proposed that the slow gating of type II BK would preclude these channels from contributing to membrane repolarization, resulting in broader APs (Brenner et al., 2005; Jaffe et al., 2011). In this case, a reduction of firing rate is observed due to activation of small conductance Ca^{2+}-activated K^+ (SK) channels (Brenner et al., 2005). On the other hand, at high Ca^{2+} concentrations (>10 µM Ca^{2+}), activation of β_4-containing type II BK channels leads to significantly prolonged

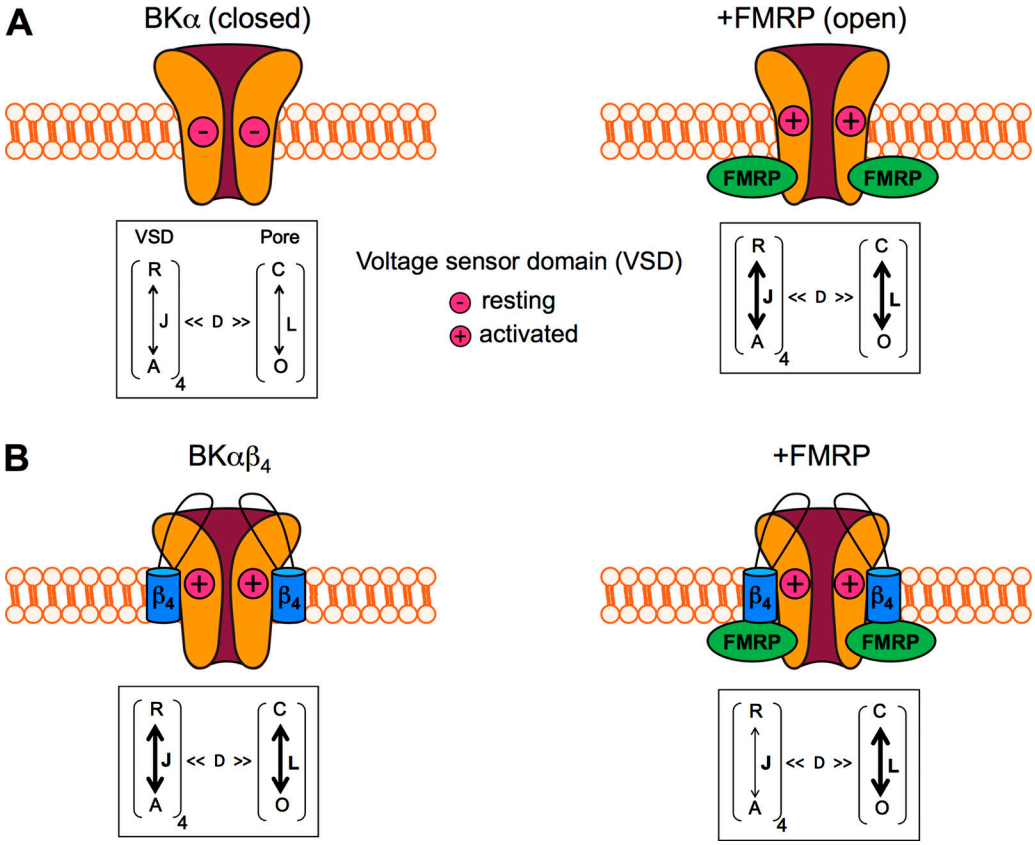

Figure 9. **Schematic model summarizing the effects of FMRP on BKα and BKαβ$_4$ channels in heterologous expression systems. (A)** Cartoon of closed BKα channel with voltage sensors in resting state. In the absence of Ca^{2+}, voltage sensor activation and pore opening are linked by the coupling factor D. Functional interaction of FMRP with the BKα subunit favors the active form of the voltage sensors (J-) and pore opening (L-). **(B)** BKβ$_4$ subunits enhance the active form of voltage sensors (J) and lower the equilibrium of pore opening (L). The presence of FMRP in the complex further increases Po by enhancing pore opening (L).

tail currents, enhancing the medium afterhyperpolarization. Larger afterhyperpolarizations result in increased interspike intervals, decreasing firing rates (Jaffe et al., 2011). Overall, the physiological outcome of BKβ$_4$ subunits' incorporation to BK channels would be a reduction of neuronal excitability, which may protect neurons against seizures. In CA3 neurons, it has been proposed that the mechanism underlying FMRP regulation of BK currents relies mainly on the direct interaction of FMRP with the regulatory BKβ$_4$ subunits, resulting in increased Ca^{2+}-dependent BK channel activation (Deng et al., 2013). It must be noted that despite the prominent expression of β$_4$ subunits in some brain regions such as the CA3 region of the hippocampus, a number of studies reported that some BK currents are still sensitive to iberiotoxin block, suggesting that not all BK channels contain BKβ$_4$ subunits (Raffaelli et al., 2004; Shruti et al., 2012; Deng et al., 2013). Interestingly, based on the biophysical and pharmacological properties of BK channel currents from CA3 neurons, Shruti et al. (2012) proposed that the main function of the BKβ$_4$ subunit is the control of BKα trafficking to the membrane. Within this physiological context, our finding that FMRP can regulate BK channels formed by BKα subunits may be of important relevance. The data that we present now suggest that in some physiological contexts FMRP may also exert similar regulatory effects by interacting with iberiotoxin-sensitive BKα-only channels. In fact, this result is consistent with previously published data showing that the FMRP effect on CA3 neuronal excitability is iberiotoxin-sensitive (Deng et al., 2013), as well as with further evidence proving interaction of BKα and FMRP in a pull-down protein assay (Myrick et al., 2015). One speculation is that the slow gating induced by FMRP would reduce the contribution of BKα channels (type I) to the AP repolarization or contribute to sustained interspike conductance. Similar to the effects on type II BK channels, the observed effects of FMRP on BKα channels are consistent with a functional effect of AP broadening, indirectly enhancing the Ca^{2+} influx and thereby increasing neurotransmitter release. However, the role of other conductances, including SK channels (Deng et al., 2019), must also be taken into account to fully understand the in vivo physiological framework depicting the regulation of electrical activity by FMRP.

Acknowledgments

Merritt C. Maduke served as editor.

We thank Prof. Mark Hollywood (Dundalk Institute of Technology, Dundalk, Ireland) for providing the BKβ$_4$ construct and for critical reading of the manuscript. We also thank David Bartolomé Martín for technical help with the representation of

STORM data and Dr. Carlo Manzo for assessment of the scripts development and validation.

This work was funded by the European Research Council under the European Union's Horizon 2020 Research and Innovation Program (grant 648936, to T. Giraldez) and Dirección de Investigaciones Científicas y Tecnológicas, Universidad de Santiago de Chile (FONDECYT 1130904 to P. Rojas).

The authors declare no competing financial interests.

Author contributions: A. Kshatri performed conceptualization, investigation, formal analysis, writing-original draft, writing-review and editing, and visualization. A. Cerrada performed investigation, formal analysis, and writing-original draft. R. Gimeno provided software and formal analysis. D. Bartolomé-Martín performed formal analysis, writing-review and editing, and validation. P. Rojas performed formal analysis and writing-review and editing. T. Giraldez provided conceptualization, formal analysis, writing-original draft, writing-review and editing, funding acquisition, supervision, visualization, project administration, and validation.

Submitted: 30 September 2019
Accepted: 12 March 2020

References

Atkinson, N.S., G.A. Robertson, and B. Ganetzky. 1991. A component of calcium-activated potassium channels encoded by the Drosophila slo locus. *Science.* 253:551–555. https://doi.org/10.1126/science.1857984

Babbey, C.M., N. Ahktar, E. Wang, C.C. Chen, B.D. Grant, and K.W. Dunn. 2006. Rab10 regulates membrane transport through early endosomes of polarized Madin-Darby canine kidney cells. *Mol. Biol. Cell.* 17:3156–3175. https://doi.org/10.1091/mbc.e05-08-0799

Bagni, C., and W.T. Greenough. 2005. From mRNP trafficking to spine dysmorphogenesis: the roots of fragile X syndrome. *Nat. Rev. Neurosci.* 6: 376–387. https://doi.org/10.1038/nrn1667

Bassell, G.J., and S.T. Warren. 2008. Fragile X syndrome: loss of local mRNA regulation alters synaptic development and function. *Neuron.* 60: 201–214. https://doi.org/10.1016/j.neuron.2008.10.004

Bear, M.F., K.M. Huber, and S.T. Warren. 2004. The mGluR theory of fragile X mental retardation. *Trends Neurosci.* 27:370–377. https://doi.org/10.1016/j.tins.2004.04.009

Behrens, R., A. Nolting, F. Reimann, M. Schwarz, R. Waldschütz, and O. Pongs. 2000. hKCNMB3 and hKCNMB4, cloning and characterization of two members of the large-conductance calcium-activated potassium channel beta subunit family. *FEBS Lett.* 474:99–106. https://doi.org/10.1016/S0014-5793(00)01584-2

Bielefeldt, K., J.L. Rotter, and M.B. Jackson. 1992. Three potassium channels in rat posterior pituitary nerve terminals. *J. Physiol.* 458:41–67. https://doi.org/10.1113/jphysiol.1992.sp019405

Brenner, R., T.J. Jegla, A. Wickenden, Y. Liu, and R.W. Aldrich. 2000. Cloning and functional characterization of novel large conductance calcium-activated potassium channel beta subunits, hKCNMB3 and hKCNMB4. *J. Biol. Chem.* 275:6453–6461. https://doi.org/10.1074/jbc.275.9.6453

Brenner, R., Q.H. Chen, A. Vilaythong, G.M. Toney, J.L. Noebels, and R.W. Aldrich. 2005. BK channel beta4 subunit reduces dentate gyrus excitability and protects against temporal lobe seizures. *Nat. Neurosci.* 8: 1752–1759. https://doi.org/10.1038/nn1573

Brown, V., P. Jin, S. Ceman, J.C. Darnell, W.T. O'Donnell, S.A. Tenenbaum, X. Jin, Y. Feng, K.D. Wilkinson, J.D. Keene, et al. 2001. Microarray identification of FMRP-associated brain mRNAs and altered mRNA translational profiles in fragile X syndrome. *Cell.* 107:477–487. https://doi.org/10.1016/S0092-8674(01)00568-2

Brown, M.R., J. Kronengold, V.R. Gazula, Y. Chen, J.G. Strumbos, F.J. Sigworth, D. Navaratnam, and L.K. Kaczmarek. 2010. Fragile X mental retardation protein controls gating of the sodium-activated potassium channel Slack. *Nat. Neurosci.* 13:819–821. https://doi.org/10.1038/nn.2563

Budelli, G., Y. Geng, A. Butler, K.L. Magleby, and L. Salkoff. 2013. Properties of Slo1 K+ channels with and without the gating ring. *Proc. Natl. Acad. Sci. USA.* 110:16657–16662. https://doi.org/10.1073/pnas.1313433110

Butler, A., S. Tsunoda, D.P. McCobb, A. Wei, and L. Salkoff. 1993. mSlo, a complex mouse gene encoding "maxi" calcium-activated potassium channels. *Science.* 261:221–224. https://doi.org/10.1126/science.7687074

Chen, L., S.W. Yun, J. Seto, W. Liu, and M. Toth. 2003. The fragile X mental retardation protein binds and regulates a novel class of mRNAs containing U rich target sequences. *Neuroscience.* 120:1005–1017. https://doi.org/10.1016/S0306-4522(03)00406-8

Chen, E., M.R. Sharma, X. Shi, R.K. Agrawal, and S. Joseph. 2014. Fragile X mental retardation protein regulates translation by binding directly to the ribosome. *Mol. Cell.* 54:407–417. https://doi.org/10.1016/j.molcel.2014.03.023

Contreras, G.F., A. Neely, O. Alvarez, C. Gonzalez, and R. Latorre. 2012. Modulation of BK channel voltage gating by different auxiliary β subunits. *Proc. Natl. Acad. Sci. USA.* 109:18991–18996. https://doi.org/10.1073/pnas.1216953109

Darnell, J.C., K.B. Jensen, P. Jin, V. Brown, S.T. Warren, and R.B. Darnell. 2001. Fragile X mental retardation protein targets G quartet mRNAs important for neuronal function. *Cell.* 107:489–499. https://doi.org/10.1016/S0092-8674(01)00566-9

Deng, P.Y., and V.A. Klyachko. 2016. Genetic upregulation of BK channel activity normalizes multiple synaptic and circuit defects in a mouse model of fragile X syndrome. *J. Physiol.* 594:83–97. https://doi.org/10.1113/JP271031

Deng, P.Y., Z. Rotman, J.A. Blundon, Y. Cho, J. Cui, V. Cavalli, S.S. Zakharenko, and V.A. Klyachko. 2013. FMRP regulates neurotransmitter release and synaptic information transmission by modulating action potential duration via BK channels. *Neuron.* 77:696–711. https://doi.org/10.1016/j.neuron.2012.12.018

Deng, P.Y., D. Carlin, Y.M. Oh, L.K. Myrick, S.T. Warren, V. Cavalli, and V.A. Klyachko. 2019. Voltage-Independent SK-Channel Dysfunction Causes Neuronal Hyperexcitability in the Hippocampus of *Fmr1* Knock-Out Mice. *J. Neurosci.* 39:28–43. https://doi.org/10.1523/JNEUROSCI.1593-18.2018

Devys, D., Y. Lutz, N. Rouyer, J.P. Bellocq, and J.L. Mandel. 1993. The FMR-1 protein is cytoplasmic, most abundant in neurons and appears normal in carriers of a fragile X premutation. *Nat. Genet.* 4:335–340. https://doi.org/10.1038/ng0893-335

Dunn, K.W., M.M. Kamocka, and J.H. McDonald. 2011. A practical guide to evaluating colocalization in biological microscopy. *Am. J. Physiol. Cell Physiol.* 300:C723–C742. https://doi.org/10.1152/ajpcell.00462.2010

Faber, E.S., and P. Sah. 2003. Ca2+-activated K+ (BK) channel inactivation contributes to spike broadening during repetitive firing in the rat lateral amygdala. *J. Physiol.* 552:483–497. https://doi.org/10.1113/jphysiol.2003.050120

Fähling, M., R. Mrowka, A. Steege, K.M. Kirschner, E. Benko, B. Förstera, P.B. Persson, B.J. Thiele, J.C. Meier, and H. Scholz. 2009. Translational regulation of the human achaete-scute homologue-1 by fragile X mental retardation protein. *J. Biol. Chem.* 284:4255–4266. https://doi.org/10.1074/jbc.M807354200

Ferron, L. 2016. Fragile X mental retardation protein controls ion channel expression and activity. *J. Physiol.* 594:5861–5867. https://doi.org/10.1113/JP270675

Ferron, L., M. Nieto-Rostro, J.S. Cassidy, and A.C. Dolphin. 2014. Fragile X mental retardation protein controls synaptic vesicle exocytosis by modulating N-type calcium channel density. *Nat. Commun.* 5:3628. https://doi.org/10.1038/ncomms4628

Gonzalez-Perez, V., and C.J. Lingle. 2019. Regulation of BK Channels by Beta and Gamma Subunits. *Annu. Rev. Physiol.* 81:113–137. https://doi.org/10.1146/annurev-physiol-022516-034038

Hamill, O.P., A. Marty, E. Neher, B. Sakmann, and F.J. Sigworth. 1981. Improved patch-clamp techniques for high-resolution current recording from cells and cell-free membrane patches. *Pflugers Arch.* 391:85–100. https://doi.org/10.1007/BF00656997

Horrigan, F.T., and R.W. Aldrich. 2002. Coupling between voltage sensor activation, Ca2+ binding and channel opening in large conductance (BK) potassium channels. *J. Gen. Physiol.* 120:267–305. https://doi.org/10.1085/jgp.20028605

Jaffe, D.B., B. Wang, and R. Brenner. 2011. Shaping of action potentials by type I and type II large-conductance Ca^{2}+-activated K+ channels. *Neuroscience.* 192:205–218. https://doi.org/10.1016/j.neuroscience.2011.06.028

Knaus, H.G., A. Eberhart, H. Glossmann, P. Munujos, G.J. Kaczorowski, and M.L. Garcia. 1994. Pharmacology and structure of high conductance calcium-activated potassium channels. *Cell. Signal.* 6:861–870. https://doi.org/10.1016/0898-6568(94)90019-1

Kshatri, A.S., A. Gonzalez-Hernandez, and T. Giraldez. 2018. Physiological roles and therapeutic potential of Ca^{2+} activated potassium channels in the nervous system. *Front. Mol. Neurosci.* 11:258. https://doi.org/10.3389/fnmol.2018.00258

Large, R.J., A. Kshatri, T.I. Webb, S. Roy, A. Akande, E. Bradley, G.P. Sergeant, K.D. Thornbury, N.G. McHale, and M.A. Hollywood. 2015. Effects of the novel BK (KCa 1.1) channel opener GoSlo-SR-5-130 are dependent on the presence of BKβ subunits. *Br. J. Pharmacol.* 172:2544–2556. https://doi.org/10.1111/bph.13085

Latorre, R., K. Castillo, W. Carrasquel-Ursulaez, R.V. Sepulveda, F. Gonzalez-Nilo, C. Gonzalez, and O. Alvarez. 2017. Molecular Determinants of BK Channel Functional Diversity and Functioning. *Physiol. Rev.* 97:39–87. https://doi.org/10.1152/physrev.00001.2016

Ma, Z., X.J. Lou, and F.T. Horrigan. 2006. Role of charged residues in the S1-S4 voltage sensor of BK channels. *J. Gen. Physiol.* 127:309–328. https://doi.org/10.1085/jgp.200509421

Meera, P., M. Wallner, and L. Toro. 2000. A neuronal beta subunit (KCNMB4) makes the large conductance, voltage- and Ca2+-activated K+ channel resistant to charybdotoxin and iberiotoxin. *Proc. Natl. Acad. Sci. USA.* 97:5562–5567. https://doi.org/10.1073/pnas.100118597

Myrick, L.K., P.Y. Deng, H. Hashimoto, Y.M. Oh, Y. Cho, M.J. Poidevin, J.A. Suhl, J. Visootsak, V. Cavalli, P. Jin, et al. 2015. Independent role for presynaptic FMRP revealed by an FMR1 missense mutation associated with intellectual disability and seizures. *Proc. Natl. Acad. Sci. USA.* 112:949–956. https://doi.org/10.1073/pnas.1423094112

Orio, P., P. Rojas, G. Ferreira, and R. Latorre. 2002. New disguises for an old channel: MaxiK channel beta-subunits. *News Physiol. Sci.* 17:156–161.

Raffaelli, G., C. Saviane, M.H. Mohajerani, P. Pedarzani, and E. Cherubini. 2004. BK potassium channels control transmitter release at CA3-CA3 synapses in the rat hippocampus. *J. Physiol.* 557:147–157. https://doi.org/10.1113/jphysiol.2004.062661

Reinhart, P.H., and I.B. Levitan. 1995. Kinase and phosphatase activities intimately associated with a reconstituted calcium-dependent potassium channel. *J. Neurosci.* 15:4572–4579. https://doi.org/10.1523/JNEUROSCI.15-06-04572.1995

Reinhart, P.H., S. Chung, and I.B. Levitan. 1989. A family of calcium-dependent potassium channels from rat brain. *Neuron.* 2:1031–1041. https://doi.org/10.1016/0896-6273(89)90227-4

Ricci, M.A., C. Manzo, M.F. García-Parajo, M. Lakadamyali, and M.P. Cosma. 2015. Chromatin fibers are formed by heterogeneous groups of nucleosomes in vivo. *Cell.* 160:1145–1158. https://doi.org/10.1016/j.cell.2015.01.054

Robitaille, R., and M.P. Charlton. 1992. Presynaptic calcium signals and transmitter release are modulated by calcium-activated potassium channels. *J. Neurosci.* 12:297–305. https://doi.org/10.1523/JNEUROSCI.12-01-00297.1992

Robitaille, R., M.L. Garcia, G.J. Kaczorowski, and M.P. Charlton. 1993. Functional colocalization of calcium and calcium-gated potassium channels in control of transmitter release. *Neuron.* 11:645–655. https://doi.org/10.1016/0896-6273(93)90076-4

Shintani, M., T. Yoshida, H. Habe, T. Omori, and H. Nojiri. 2005. Large plasmid pCAR2 and class II transposon Tn4676 are functional mobile genetic elements to distribute the carbazole/dioxin-degradative car gene cluster in different bacteria. *Appl. Microbiol. Biotechnol.* 67:370–382. https://doi.org/10.1007/s00253-004-1778-0

Shruti, S., J. Urban-Ciecko, J.A. Fitzpatrick, R. Brenner, M.P. Bruchez, and A.L. Barth. 2012. The brain-specific Beta4 subunit downregulates BK channel cell surface expression. *PLoS One.* 7:e33429. https://doi.org/10.1371/journal.pone.0033429

Sigg, D., and F. Bezanilla. 1997. Total charge movement per channel. The relation between gating charge displacement and the voltage sensitivity of activation. *J. Gen. Physiol.* 109:27–39. https://doi.org/10.1085/jgp.109.1.27

Uebele, V.N., A. Lagrutta, T. Wade, D.J. Figueroa, Y. Liu, E. McKenna, C.P. Austin, P.B. Bennett, and R. Swanson. 2000. Cloning and functional expression of two families of beta-subunits of the large conductance calcium-activated K+ channel. *J. Biol. Chem.* 275:23211–23218. https://doi.org/10.1074/jbc.M910187199

Wallner, M., P. Meera, and L. Toro. 1999. Molecular basis of fast inactivation in voltage and Ca2+-activated K+ channels: a transmembrane beta-subunit homolog. *Proc. Natl. Acad. Sci. USA.* 96:4137–4142. https://doi.org/10.1073/pnas.96.7.4137

Wang, B., B.S. Rothberg, and R. Brenner. 2006. Mechanism of beta4 subunit modulation of BK channels. *J. Gen. Physiol.* 127:449–465. https://doi.org/10.1085/jgp.200509436

Wang, T., S.M. Bray, and S.T. Warren. 2012. New perspectives on the biology of fragile X syndrome. *Curr. Opin. Genet. Dev.* 22:256–263. https://doi.org/10.1016/j.gde.2012.02.002

Webb, T.I., A.S. Kshatri, R.J. Large, A.M. Akande, S. Roy, G.P. Sergeant, N.G. McHale, K.D. Thornbury, and M.A. Hollywood. 2015. Molecular mechanisms underlying the effect of the novel BK channel opener GoSlo: involvement of the S4/S5 linker and the S6 segment. *Proc. Natl. Acad. Sci. USA.* 112:2064–2069. https://doi.org/10.1073/pnas.1400555112

Whitt, J.P., J.R. Montgomery, and A.L. Meredith. 2016. BK channel inactivation gates daytime excitability in the circadian clock. *Nat. Commun.* 7:10837. https://doi.org/10.1038/ncomms10837

Willemsen, R., M. Hoogeveen-Westerveld, S. Reis, J. Holstege, L.A. Severijnen, I.M. Nieuwenhuizen, M. Schrier, L. van Unen, F. Tassone, A.T. Hoogeveen, et al. 2003. The FMR1 CGG repeat mouse displays ubiquitin-positive intranuclear neuronal inclusions; implications for the cerebellar tremor/ataxia syndrome. *Hum. Mol. Genet.* 12:949–959. https://doi.org/10.1093/hmg/ddg114

Xia, X.M., J.P. Ding, and C.J. Lingle. 1999. Molecular basis for the inactivation of Ca2+- and voltage-dependent BK channels in adrenal chromaffin cells and rat insulinoma tumor cells. *J. Neurosci.* 19:5255–5264. https://doi.org/10.1523/JNEUROSCI.19-13-05255.1999

Zanacchi, F.C., C. Manzo, A.S. Alvarez, N.D. Derr, M.F. Garcia-Parajo, and M. Lakadamyali. 2017. A DNA origami platform for quantifying protein copy number in super-resolution. *Nat. Methods.* 14:789–792. https://doi.org/10.1038/nmeth.4342

Zhang, J., C.M. Carver, F.S. Choveau, and M.S. Shapiro. 2016. Clustering and Functional coupling of diverse ion channels and signaling proteins revealed by super-resolution STORM microscopy in neurons. *Neuron.* 92:461–478. https://doi.org/10.1016/j.neuron.2016.09.014

Supplemental material

Supplementary Methods

Quantitative analysis of STORM images

Quantitative analysis of dSTORM data was performed using customized algorithms implemented with Python. The molecule lists were exported from NIS-Elements software, and drift-corrected coordinates "X" and "Y" were collected separately for Alexa Fluor 647 and Alexa Fluor 488 localizations. These values were input in our algorithm to calculate the NND of each molecule with respect to others labeled with the same fluorophore or with the other. GraphPad Prism version 7.00 (GraphPad Software) was used to plot histograms representing the distribution (in percentage) of the calculated NND. In-house software written in Python was additionally used to identify and calculate areas of clusters with all possible protein combinations in each experimental condition. This analysis used the DBSCAN algorithm, a data-clustering algorithm that finds core samples of high density and expands clusters from them. This algorithm is based on two parameters: "epsilon" (radius) and minimum number of particles (min_pts). Experimentally, we concluded that 60 nm and 10 particles were the values that permit the clearance of most of the background nonspecific signals but with the minimum loss of information. Data were represented as histograms using Spyder v.3.3.1, an open-source scientific Python development environment.

Control of STORM analysis

We implemented a control experiment to verify that our analyzed STORM data correspond to real formation of complexes between the labeled proteins and not to random co-localization of the fluorophores. In this context, a common strategy is to rotate the image of one channel, thus modifying the relative position between proteins without altering relative coexpression or labeling levels (Babbey et al., 2006; Dunn et al., 2011).

We used a real two-channel molecule list and its corresponding reconstructed image (particles represented as green dots or red dots; Fig. S1). NND analysis resulted in a distribution of distance values between particles from both channels showing a high peak at around 60 nm (Fig. S1 C, blue bars). The cluster analysis yielded 218 "647-labeled clusters," 145 "488-labeled clusters," and 271 "combined clusters" (histogram in Fig. S1 D, left panel).

Using the same molecule list, the positions in the green channel were modified by rotating the field 90° clockwise and applying a vertical flip (Fig. S1 B), and the new disposition of particles was analyzed again. In this case, the distribution of distances between particles of both channels obtained by NND analysis was broadly distributed at higher distance values (Fig. S1 C, orange bars). Consistent with this, cluster analysis yielded only 25 combined clusters compared with 271 from the original data (Fig. S1 D, right panel). Altogether, these results suggest that the distribution of clusters obtained in the original data are not arbitrary but are a consequence of the interaction between proteins.

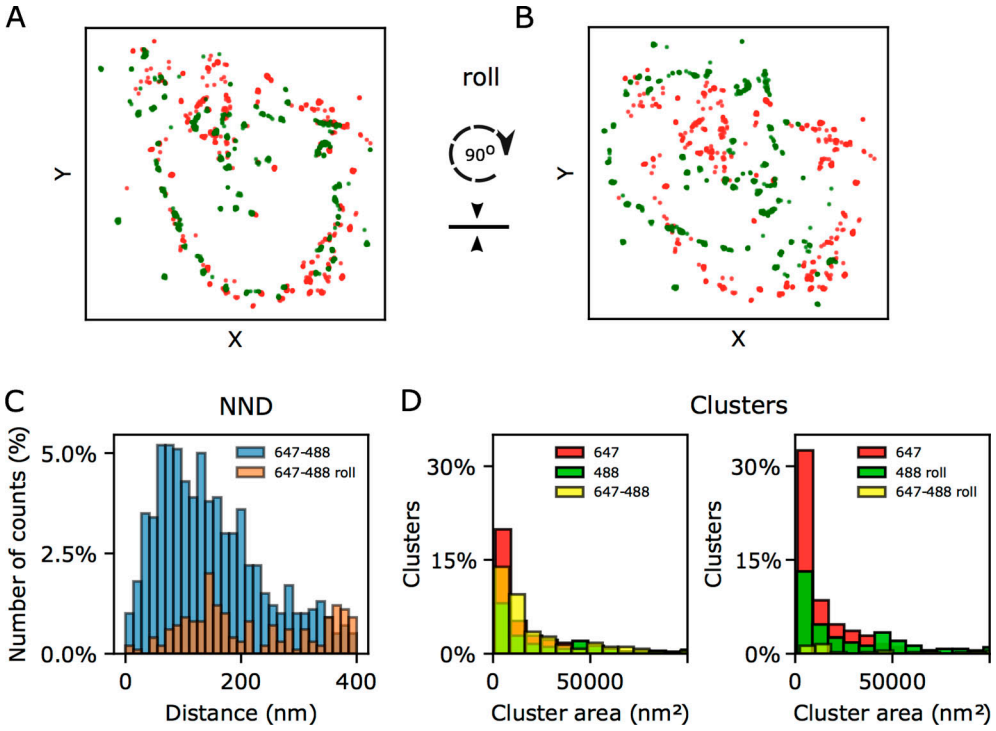

Figure S1. **STORM analysis control. (A and B)** STORM reconstructed image before (A) and after (B) rolling (90° rotation) and flipping of the "488" channel (particles represented as red or green dots). **(C)** NND analysis performed before (blue) and after (orange) rotating/flipping of the green channel. **(D)** Cluster analysis before (left panel) and after (right panel) rotating/flipping of the green channel.